QBOi El Nino Southern Oscillation experiments
Part I: Overview of experiment design and ENSO modulation of the QBO

Yoshio Kawatani[1,2], Kevin Hamilton[3], Shingo Watanabe[2], James A. Anstey[4], Jadwiga H. Richter[5], Neal Butchart[6], Clara Orbe[7], Scott M. Osprey[8], Hiroaki Naoe[9], Dillon Elsbury[10,11], Chih-Chieh Chen[5], Javier García-Serrano[12,13], Anne Glanville[5], Tobias Kerzenmacher[14], François Lott[15], Froila M. Palmerio[12,16], Mijeong Park[5], Federico Serva[17], Masakazu Taguchi[18], Stefan Versick[14], Kohei Yoshida[9]

[1]Faculty of Environmental Earth Science, Hokkaido University, Sapporo, Japan
[2]Japan Agency for Marine-Earth Science and Technology, Yokohama, Japan
[3]International Pacific Research Center and Department of Atmospheric Sciences, University of Hawaii, Honolulu, USA
[4]Canadian Centre for Climate Modelling and Analysis (CCCma), Victoria BC, Canada
[5]U. S. National Science Foundation National Center for Atmospheric Research (NSF NCAR), Boulder, CO, USA
[6]Met Office Hadley Centre, Exeter, UK
[7]NASA Goddard Institute for Space Studies (GISS), New York, USA
[8]National Centre for Atmospheric Science (NCAS), University of Oxford, Oxford, UK
[9]Meteorological Research Institute (MRI), Tsukuba, Japan
[10] Cooperative Institute for Research in Environmental Sciences, University of Colorado Boulder, Boulder, Colorado
[11]NOAA/Chemical Sciences Laboratory, Boulder, Colorado
[12] Group of Meteorology, Universitat de Barcelona, Barcelona, Spain
[13]Barcelona Supercomputing Center (BSC), Barcelona, Spain
[14]Institute of Meteorology and Climate Research–Atmospheric Trace Gases and Remote Sensing (IMK-ASF) Karlsruhe Institute of Technology (KIT), Karlsruhe, Germany
[15]Laboratorie de Météorologie Dynamique (LMD), Paris, France
[16]CMCC Foundation - Euro-Mediterranean Center on Climate Change, Italy.
[17]Institute of Marine Sciences, National Research Council (ISMAR-CNR), Rome, Italy
[18]Aichi University of Education, Kariya, Japan

Correspondence to: Yoshio Kawatani (kawatani@ees.hokudai.ac.jp)

Abstract

40 Stratosphere-troposphere Processes And their Role in Climate (SPARC) Quasi-Biennial Oscillation initiative (QBOi) project has conducted new experiments to explore the modulation of the QBO by El Niño-Southern Oscillation (ENSO). This paper provides an overview of the experiment design and investigates the modulation of the QBO by ENSO using nine climate models from the QBOi. A key finding is a consistent lengthening of the QBO period during La Niña compared to El Niño across all models, aligning with observational evidence. However, the magnitude of this lengthening shows large intermodel

45 differences. By contrast, even the sign of the ENSO effect on QBO amplitude varies among models -models employing variable parameterized gravity wave sources generally exhibit greater sensitivity of the QBO amplitude to the presence of ENSO than those models using fixed sources. The models capture key observed ENSO-related characteristics, including a weaker Walker circulation and increased equatorial precipitation during El Niño compared to La Niña, as well as a characteristic response in zonal mean zonal wind and temperature. These modulations influence the propagation and filtering

50 of gravity waves. Notably, models with variable parameterized gravity wave sources show stronger wave forcing during El Niño, potentially explaining the shorter QBO period modulation in these models. Further investigation into the complex interplay between ENSO, gravity waves, and the QBO can contribute to improved model formulations.

1 Introduction

55 The familiar Quasi-Biennial Oscillation (QBO), characterized by alternating easterly and westerly prevailing stratospheric winds in the tropics, dominates the large-scale circulation of the tropical stratosphere. The QBO influences the stratospheric polar vortex by modulating the propagation of extratropical planetary waves, consequently impacting storm tracks and surface pressure patterns in mid-to-high latitudes (Baldwin and Dunkerton, 2001; Anstey and Shepherd 2014; Kidston et al., 2015). In the equatorial troposphere, the Madden-Julian Oscillation (MJO), a large-scale tropical cloud activity

60 pattern, may exhibit enhanced activity during the QBO easterly phase at 50 hPa (Yoo and Son, 2015). Other QBO-related effects beyond the tropical stratosphere may include the modulation of the mid-latitude subtropical jet by off-equatorial secondary circulations, filtering of propagating gravity waves into the upper stratosphere and mesosphere that then affect the Semiannual Oscillation (SAO) near and above the stratopause and even acting to generate a mesopause QBO (MQBO) (Baldwin et al., 2001; Anstey et al., 2022). Indeed recent research indicates that QBO facilitates troposphere-stratosphere

65 coupling and influences a wide range of dynamical and chemical processes spanning the equator to the poles and from the surface to the mesopause (Anstey et al., 2022).

The QBO in equatorial prevailing wind has been observed (at least up to mid-stratospheric levels) for over seven decades (Naujokat, 1986). It is clear over this record that the QBO differs somewhat from cycle to cycle (e.g. Quiroz, 1981) and there have been efforts to try to see if the cycle-to-cycle variations may systematically depend on such factors as solar

70 activity, volcanic eruptions or the El Niño/Southern Oscillation (ENSO) cycle of the tropical troposphere (Dunkerton, 1983; Geller et al., 1997; Salby and Callahan, 2000; Hamilton, 2002, Kane, 2004; Taguchi, 2010). It seems that the strongest empirical connection that has been observed is between the QBO period and the ENSO phase. Notably Taguchi (2010)

analyzed radiosonde observations of zonal wind from 70 hPa to 10 hPa over Singapore (1.3°N) for the period 1953-2008. He found that QBO signals exhibit faster phase propagation during El Niño compared to La Niña conditions, along with a weaker

75   QBO amplitude during El Niño. Yuan et al. (2014) largely confirmed these findings using radiosonde data from ten near-equatorial stations but noted that the ENSO influence on the QBO amplitude appears less robust than its influence on the QBO period.

The present paper will discuss our investigation of the dynamics of the ENSO-QBO connection, using simulations from comprehensive global atmospheric general circulation models (AGCMs). First, we very briefly review here some key

80   aspects of the current understanding of the dynamics of the QBO and its representation in AGCMs. The QBO is believed to be primarily driven by atmospheric waves, predominantly gravity waves generated by tropical cumulus convection. Eastward and westward propagating gravity waves, excited by active convection in the equatorial regions, propagate vertically from the troposphere to the stratosphere. Upon dissipation, they deposit mean momentum into the background zonal wind, accelerating it and generating the westerly (eastward wind) and easterly (westward wind) phases of the QBO, respectively. Large-scale

85   Kelvin waves and inertia-gravity waves contribute to the QBO westerly acceleration phase, while small-scale gravity waves primarily drive the easterly accelerations (Hamilton et al., 1999; Kawatani et al., 2010a, 2010b; Evan et al., 2012).

Some global climate models with moderate horizontal and vertical resolutions have been able to simulate the QBO by representing the effects of sub-grid scale non-orographic gravity waves through parameterization. However, despite advancements in observational techniques, our understanding of the gravity wave field in the tropical stratosphere remains

90   limited, hindering our ability to fully determine their geographical distribution, temporal variations, and sources (e.g., Alexander et al., 2010). Consequently, non-orographic gravity wave parameterizations (GWPs) must rely on simplified physical assumptions, frequently assuming constant gravity wave sources and/or launch levels in space and time.

The Brewer-Dobson mean meridional circulation (BDC) in the stratosphere, ascends in the equatorial region, flows poleward toward both hemispheres, and descends at high latitudes. The equatorial upwelling within the BDC can slow down

95   or even temporarily halt the downward propagation of the QBO phase as it descends from the upper to the lower stratosphere. Generally, shorter QBO periods are associated with stronger zonal wave forcing and/or weaker tropical upwelling, and vice versa (Dunkerton, 1997). Previous research suggests that tropical upwelling is actually stronger during El Niño (Randel et al., 2009; Calvo et al., 2010; Simpson et al., 2011). Therefore, it seems likely that the shorter QBO periods observed during El Niño result from increased wave driving of the mean flow accelerations (Schirber, 2015; Kawatani et al., 2019).

100   Stratosphere-troposphere Processes And their Role in Climate (SPARC) Quasi-Biennial Oscillation initiative (QBOi), launched in 2015 (Anstey et al. 2022; Butchart et al., 2018), aims to compare the representation of the QBO in climate models and comprises five core papers in its first phase (note that SPARC was renamed to APARC, Atmosphere Processes And their Role in Climate, in January 2024). These papers focused on: (1) evaluating the QBO in participating AGCMs (Bushell et al., 2020); (2) investigating the QBO's response to a warming climate (Richter et al., 2020); (3) evaluating tropical waves and their

105   forcing of the QBO (Holt et al., 2020); (4) investigating QBO teleconnections (Anstey et al., 2021); and (5) evaluating seasonal forecast prediction skills for the QBO (Stockdale et al., 2020).

For paper 2, eleven climate models participated in a global warming experiment (doubled CO_2 and globally uniform +2K SST increase, and a quadrupled CO_2 experiment with a +4K SST increase). Consistent with previous studies (Kawatani et al., 2011; Watanabe and Kawatani, 2012; Kawatani and Hamilton, 2013), all models showed a weakening of the QBO

110 amplitude in the lower stratosphere with global warming. However, significant variability existed among models regarding changes in the QBO period. Recent global warming experiments using climate models have produced mixed results regarding the QBO period under increasing CO_2 and SST conditions. Some models project a shorter period, others a longer period, and still others project no change or even the disappearance of the QBO in the warmer mean climate (Richter et al., 2020; Butchart et al., 2020; DallaSanta et al. 2021). This discrepancy may stem from differing assumptions regarding GWP in different models,

115 in addition to varying responses of resolved waves, precipitation, and large-scale circulations like the BDC and Walker circulations (Richter et al., 2020). It is worth noting that the tropical Pacific circulation response to warming has an El Niño like pattern (Vecchi and Soden, 2007), while this is not the case for the extratropical circulation (Lu et al., 2008).

While almost all climate models incorporate non-orographic GWP to simulate the QBO, most fix the sources of parameterized gravity waves, implying that gravity wave activity remains unaffected by changes in SSTs and CO_2

120 concentration. However, some recent models utilize GWP with variable sources linked to cumulus convection, reflecting the real-world relationship between convective activity and gravity wave generation. Verifying the modulation of resolved and parameterized waves in a future climate is impossible. However, investigating how the simulated QBO is modulated in individual models under El Niño and La Niña conditions is feasible.

The MIROC model without non-orographic GWP has successfully simulated the QBO by utilizing higher vertical

125 resolution (~300 m or 550 m) and a modified Arakawa-Schubert type cumulus parameterization (e.g., Kawatani et al., 2005; Watanabe et al., 2008; Kawatani et al., 2011). Kawatani et al. (2019) conducted an ENSO-QBO experiment using the MIROC-AGCM with 100-year integrations of both El Niño and La Niña conditions, which simulated a shorter QBO period during El Niño compared to La Niña, consistent with the observations of Taguchi (2010) and Yuan et al. (2014). Kawatani et al. (2019) found that in their AGCM equatorial upwelling associated with the BDC strengthens during El Niño, and gravity waves

130 contributing to the QBO become more prominent due to increased precipitation directly above the equator. Analyses based on Transformed Eulerian Mean (TEM) equations revealed that the effect of gravity waves overcomes that of tropical upwelling, leading to a shorter QBO period during El Niño compared to La Niña. Furthermore, Kawatani et al. (2019) conducted spectral analyses of high temporal and spatial resolution satellite cloud observational data (CLAUS, TRMM), revealing that convective activity in the spectral domain with slow horizontal phase speeds (say less than about 10 m s^{-1}) is more pronounced during El

135 Niño compared to La Niña – a characteristic also qualitatively simulated in the MIROC-AGCM. This modulation of convective activity results in the excitation of more slow-phase-speed gravity waves during El Niño, facilitating the QBO descent to the lower stratosphere. Additionally, the generally weaker Walker circulation during El Niño compared to La Niña creates favorable conditions for gravity waves generated in the troposphere to propagate into the stratosphere and effectively drive the QBO.

140   Conducting a common ENSO-QBO experiment across a range of QBO-resolved climate models could help elucidate the role of non-orographic GWP in driving the oscillation. This exercise would be beneficial for evaluating both GWP schemes and model responses to ENSO, particularly in terms of whether a model accurately simulates shorter QBO periods during El Niño compared to La Niña. Nine models participated in the QBOi-ENSO experiments and provided datasets. We aim to present three core papers for this project: (i) QBOi-ENSO experimental design and basic characteristics of ENSO modulation of the

145   QBO (this paper); (ii) teleconnections of the QBO during El Niño and La Niña; and (iii) Madden-Julian Oscillation modulation associated with ENSO and the QBO.

        The QBOi-ENSO experiment utilized long, continuous model integrations with annually-repeating prescribed SSTs characteristic of either El Niño or La Niña conditions, following Kawatani et al. (2019). Although this approach does not fully capture real-world SST evolution (e.g., the SST field of a mature El Niño at the end of a calendar year directly transitioning to

150   the developing phase of another El Niño in the following year), this simplified design ensures a diverse sampling of QBO phases relative to the annual cycle. Basing our prescribed SST anomalies on composites of numerous actual historical months enables us to compare our atmospheric simulations with observations under our perpetual El Niño and La Niña model runs.

        As explained in the following section, some model groups were unable to provide the complete set of model data necessary for analysis, and this limits our ability to conduct a comprehensive analysis and comparison across all models.

155   Detailed zonal-time spectral analyses of model fields, like those performed in Kawatani et al. (2019), remain a subject for future study. This paper, the first core paper of the QBOi-ENSO experiments, focuses on the representation of fundamental ENSO modulation of the QBO and discusses the possible roles of GWP in each model. This paper is structured as follows: Section 2 describes the model and experimental design. Section 3 examines ENSO modulation of the QBO and climatological differences in mean fields. Section 4 investigates wave forcing and residual mean meridional circulations in El Niño versus La

160   Niña. Finally, Section 5 summarizes the study and provides concluding remarks.

2. Model Description and Experimental Design

        The experimental design for the QBOi phase-1 project, including model names, domain and resolution, information on non-orographic gravity wave parameterization (GWP), and requested output variables, is detailed in Butchart et al. (2018).

165   QBOi experiment 2 employed repeated annual cycles of sea surface temperatures (SSTs), sea ice, and external forcings. The current ENSO-QBOi experiments follow the same framework as experiment 2 but incorporate annual cycle anomalies of El Niño and La Niña SSTs into the climatological annual cycles of SSTs.

        The prescribed SST anomalies used in these experiments were derived using the same procedure outlined in Kawatani et al. (2019). El Niño SST anomalies were calculated as a function of the time of year using AMIP SST data from 1950-2016.

170   We computed a composite SST anomaly for each calendar month averaged over all times classed as El Niño conditions. The same procedure was used to construct annually repeating La Niña SST anomalies. This ENSO state characterization follows the definitions used by the Japan Meteorological Agency (JMA). El Niño and La Niña months are selected individually for

each calendar month (i.e., each January, February, …, December) based on the JMA definition. Monthly SST data are weighted by the NINO.3 SST deviation values and then averaged.

175   The result of this procedure is a composite SST anomaly that for the NINO.3 region is 1.92 K in January. This would correspond to "moderately strong" El Niño conditions. To produce more significant effects on the QBOi model integrations, the calculated composite SST anomalies were amplified. In a change from the procedure employed by Kawatani et al. (2019), in the present study the El Niño composite anomalies were multiplied by a factor of 1.8 and the La Niña composite anomalies by a factor of 1.4. These factors bring the peak composite anomaly SSTs closer to the anomalies observed during the most

180 intense El Niño and La Niña events. This approach allows for long integrations of QBOi models with prescribed perpetual El Niño and La Niña SSTs while avoiding the introduction of other interannual variability. More detailed explanations are provided in Kawatani et al. (2019).

Figures 1a and 1b show the annual mean composite SST deviations from the climatology for El Niño and La Niña, respectively. Figures 1c and 1d depict the composite NINO.3 SST anomalies throughout the year for El Niño and La Niña,

185 respectively. To illustrate the annual cycle clearly, a two-year period is displayed (simply repeating the same composite values). The El Niño anomalies are weaker during boreal summer and intensify during boreal winter (Fig. 1c). It is important to note that the applied procedure cannot fully capture the development, mature phase, and decay of all observed El Niño events, as the evolution of an event can span more than a year. Nevertheless, the simulated time evolution generally resembles that of real events, with El Niño amplitudes tending to peak during boreal winter. La Niña, on the other hand, does not exhibit such a

190 clear standard seasonal development pattern (Fig. 1d).

The monthly El Niño and La Niña SSTs used in the model integrations are generated by adding the composite monthly SST anomaly to the monthly climatological SSTs used in the QBOi experiment 2 for each model. The imposed SSTs are the only difference between our El Niño and La Niña runs; other prescribed fields, such as sea ice and stratospheric ozone distributions, remain identical. The global average SST anomaly is +0.176 K for El Niño and -0.134 K for La Niña. These

195 differences in global mean SST are significantly smaller than those in typical global warming experiments. For instance, global SST increases of +2 K (+4 K) with doubled (quadrupled) CO_2 concentrations were utilized in QBOi experiments 3 and 4 (Richter et al., 2020).

Nine models participated in the QBOi-ENSO experiments: CESM1 (CESM15-110L), EC-EARTH3.3, ECHAM5sh, EMAC, GISS-E2-2G, LMDz6, MIROC-AGCM-LL, MIROC-ESM and MRI-ESM2.0CESM1. For clarity and conciseness,

200 we will refer to these models as CESM1, EC-EARTH, ECHAM, EMAC, GISS, LMDz, MIROC-AGCM, MIROC-ESM and MRICESM1, respectively. Table 1 summarizes the model information. Five models (EC-EARTH, ECHAM, EMAC, MIROC-ESM, and MRI) employed fixed sources of parameterized gravity waves, while three models (CESM1, GISS and LMDz) used variable sources. Launch levels for parameterized gravity waves varied across models, ranging from 450 to 700 hPa or 1000 to 100 hPa. Notably, MIROC-AGCM does not incorporate non-orographic GWP; therefore, the QBO in this model is driven

205 solely by resolved waves. Note that, while MIROC avoids the arbitrariness involved with GWP, the T106 horizontal resolution (1.125°) in this model is insufficient to represent small-scale gravity waves, which are thought to be particularly important for

driving the QBO easterly phase (Kawatani et al., 2010). Model integration periods also varied, ranging from 40 to 100 years. Climatological means were calculated using all available data. For example, in the case of GISS, which comprises three ensemble members with 30-year integrations, data from all members were analyzed separately and then averaged to create
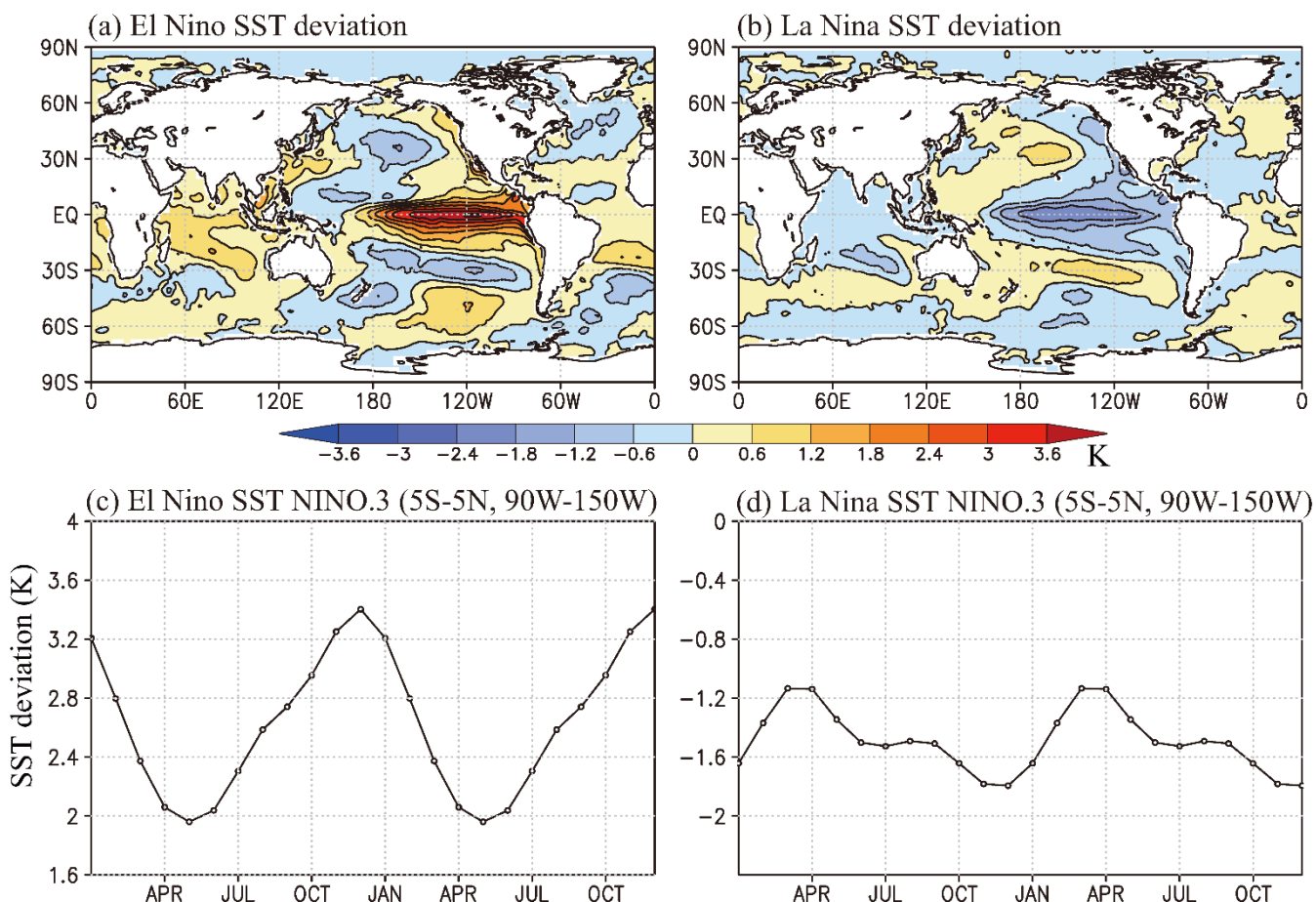210   climatological fields.

Figure 1: Annual mean composite SST deviations from climatology for the (a) El Niño and (b) La Niña composites. The contour interval is 0.6 K. The annual cycle of NINO.3 SST deviation from climatology for our (c) El Niño and (d) La Niña composites. For visualization, two full repeating cycles are shown.

215   More detailed model information for CESM1, EC-EARTH, ECHAM, EMAC, LMDz, MIROC-AGCM and MIROC-ESM can be found in Butchart et al. (2018). In the QBOi-ENSO experiment, MRI-ESM2.0 was used instead of the MRI-ESM2 described in Butchart et al. (2018). MRI-ESM2.0 (Yukimoto et al., 2019) is an updated version of the model documented in Butchart et al. (2018), and it includes changes aimed at improving the modelled QBO (Naoe and Yoshida, 2019). Updated information about EC-EARTH3.3, compared to EC-EARTH3.1 used in QBOi phase-1 (Butchart et al., 2018; Stockdale et al., 220   2020), can be found in Palmeiro et al. (2022) and Lott et al. (2024). While not included in QBOi phase-1, GISS joined the

QBOi-ENSO experiments. This model incorporates non-orographic GWP, representing gravity waves generated by convection, shear, and deformation. Refer to Rind et al. (2020) for a more detailed description of the model configuration.

Model name	Horizontal resolution	Δz (10-25 km)	non-orographic GW scheme	GWP sources	GWP lunched level	year integration
CESM1 (WACCM5-110L)	1.25°×0.94°	500 m	Richter et al. 2010	variable	1000-100 hPa	100-yr
EC-EARTH3.3	T255	0.8-1.1 km	Scinocca 2003	fixed	450 hPa	100-yr
ECHAM5sh	T63	600-700 m	Hines 1997	fixed	600 hPa	40-yr
EMAC	T42	600-700m	Hines 1997	fixed	650hPa	100-yr
GISS-E2-2G	2°×2.5°	0.5-1.0 km	Rind et al. 2007	variable	1000-100 hPa	3×30-yr
LMDz6	2°×1.25°	0.9-1.1km	Lott et al. 2012	variable	500 hPa	82-yr
MIROC-AGCM-LL	T106	550 m	–	–	–	100-yr
MIROC-ESM	T42	680 m	Hines 1997	fixed	650 hPa	100-yr
MRI-ESM2.0	T159	500-700 m	Hines 1997	fixed	700 hPa	50-yr

Table 1. Models participating in the QBOi-ENSO experiment, including information on horizontal resolution, vertical level spacing (Δz) over 10-25 km altitude, references for non-orographic gravity wave parameterizations, whether parameterized gravity wave sources are fixed or variable, launch level of parameterized gravity waves and available model integration length (years). Note that non-orographic GWP is not used in the MIROC-AGCM-LL.

The requested spatial and temporal resolution and output period align with those outlined in Butchart et al. (2018). However, a limited number of new diagnostics were added in the QBOi-ENSO experiment to facilitate the analysis of the Madden-Julian Oscillation (MJO) and the QBO-MJO teleconnection: (1) Daily variables: zonal wind, meridional wind at 200 hPa and 850 hPa, and outgoing longwave radiation (OLR) within the 30°S-30°N latitude band. (2) 3-hourly variables: OLR and precipitation. (3) 6-hourly data: temperature, zonal wind, meridional wind, and vertical wind within the 15°S-15°N latitude band, covering an altitude range of 150 to 0.4 hPa (compared to 100 to 0.4 hPa in QBOi phase-1).

While fundamental variables such as precipitation, zonal wind, and temperature were available for all models, some variables crucial for diagnosing QBO behavior were not available for some models. These include resolved wave forcing, parameterized non-orographic and orographic wave forcing, parameterized eastward and westward gravity wave fluxes, and residual mean velocity in the Transformed Eulerian Mean (TEM) equation (Table 2).

We will examine the climatological annual mean differences between the El Niño and La Niña runs across various fields. Emphasis will be placed on regions where these differences are statistically significant at a 95% confidence level. Statistical significance is determined using a two-sided Student's t-test, sampling the maximum individual yearly mean data

(e.g., 100 data points for models with 100-year integrations) for both the El Niño and La Niña runs. For comparison, zonal wind and temperature data from the ERA-Interim (ERA-I; Dee et al. 2011) reanalyses and precipitation data from the CPC Merged Analysis of Precipitation (CMAP; Xie and Arkin 1997) datasets are used. Observed El Niño and La Niña composites
245 for each calendar month were computed using reanalysis data spanning 1979-2012, consistent with the approach in Kawatani et al. (2019). The observed El Niño minus La Niña results are calculated from the annual means of these composites. Importantly, the composite ERA-I and CMAP data were not scaled by factors of 1.8 and 1.4 for El Niño and La Niña, respectively, unlike the SSTs used as boundary conditions in the QBOi model simulations, which were multiplied by these factors. Consequently, the observed El Niño minus La Niña differences are expected to be smaller than those in the QBOi
250 models. Nevertheless, these observational datasets remain valuable for evaluating the qualitative characteristics of the model differences, such as anomaly distributions.

Model name	Resolved & non-orographic GWP forcing	orographic GWP forcing	eastward/westward GWP flux	Residual stream function	$\overline{w}^*$
CESM1 (WACCM5-110L)	N/A	✓	✓	N/A	N/A
EC-EARTH3.3	N/A	N/A	N/A	N/A	✓
ECHAM5sh	✓	✓	✓	N/A	✓
EMAC	N/A	N/A	N/A	N/A	N/A
GISS-E2-2G	✓	N/A	N/A	✓5-1115	✓
LMDz6	✓	✓	N/A	✓	✓
MIROC-AGCM-LL	✓	✓	–	✓	✓
MIROC-ESM	✓	✓	✓	✓	✓
MRI-ESM2.0	✓	✓	✓	✓	✓

Table 2. Model datasets used in this study (i.e. those available as of September 2024). Datasets can include zonal momentum forcing
255 **due to resolved and non-orographic GWP, zonal forcing due to orographic GWP, eastward and westward momentum fluxes of parameterized waves, residual meridional circulation stream function, and residual vertical velocity ($\overline{w}^*$).**

3. ENSO Modulation of the QBO and Climatological Mean Field Differences

This section discusses ENSO modulation of the QBO and climatological mean field differences between the perpetual El Niño and La Niña experiments. Figure 2 shows a time-height cross-section of the monthly and zonal mean zonal
260 winds over the equator in the El Niño and La Niña simulations for each model. Red and blue colors correspond to westerlies

and easterlies, respectively. For simplicity, only results from the first 20 years of each experiment are shown. QBO-like oscillations are found in all models. In the lower stratosphere, the westerly phase duration is generally longer in the La Niña simulations compared to the El Niño simulations, particularly noticeable in EC-EARTH. The downward propagation of QBO westerly and easterly phases to the lower stratosphere is more rapid during El Niño, which is a common characteristic among the models.

In the ECHAM El Niño experiment, dominant zonal winds are westerlies above 20 hPa, easterlies at 20-30 hPa, and westerlies around 30-50 hPa. Downward phases of easterlies and westerlies occasionally occur (around years 7-10 and 13-15). These characteristics are not observed in the real atmosphere but are somewhat similar to those in their global warming experiments (i.e., QBOi phase-1 experiments 3 and 4; see Fig. 4 in Richter et al., 2020). In contrast, the ECHAM La Niña experiment simulates a much more realistic QBO with continuous downward phase propagation of both easterly and westerly phases.

In the El Niño runs, GISS and LMDz simulate rather stable QBO phases extending to the lower stratosphere, but the QBO in their La Niña experiments is more irregular, and westerly phases sometimes fail to propagate into the lower stratosphere. In GISS, westerlies are continuously formed around 50 hPa. This suggests weaker zonal wave forcing in their La Niña runs, as discussed later. Around 5-10 hPa, QBO westerly phases are much weaker in MRI, and QBO easterly phase durations are much longer than those of westerly phases. Longer easterly phases of the QBO are also visible in CESM1.

Figure 3 presents the periods of individual QBO cycles in the El Niño and La Niña runs for each model's entire integration period. For each simulated cycle, a period with an integral number of months is computed from the first month, during which the monthly and zonal mean zonal winds at 20 hPa change from westerly to easterly, to the last month, defined as one month before the next transition at 20 hPa. Note that GISS provided data for 30 years in each of its three ensemble members, which are continuously drawn in Fig. 3 (i.e., ensemble 1 starts from months 1 to 360, ensemble 2 starts from months 361 to 720, and ensemble 3 starts from months 721 to 1080 on the abscissa). The values of mean QBO period ± one standard deviation among QBO cycles are provided within each panel of Fig. 3. The simulated mean QBO period in the La Niña runs is larger than in the El Niño runs for each model, and the percentage difference relative to El Niño periods is shown at the bottom of each pair of panels (e.g., 42.5% means that QBO periods in La Niña are 1.425 times longer than those in El Niño).

Consistent with the observational study by Taguchi (2010), all models simulated longer periods during La Niña compared to El Niño runs, a difference statistically significant at the ≥ 99% confidence level for each model. However, the degree of sensitivity of the QBO periods to ENSO differs among the models. Models with relatively large percentage La Niña versus El Niño differences are EC-EARTH (42.5%), LMDz (27.9%), and ECHAM (24.6%), while those with smaller differences are EMAC (4.3%), MIROC-ESM (6.9%) and MRI (8.5%). The analysis of observed near-equatorial winds by Yuan et al. (2014) estimated long-term means for the QBO period of 25 months for El Niño conditions and 31.8 months for La Niña conditions, corresponding to a 27.2% difference.

10
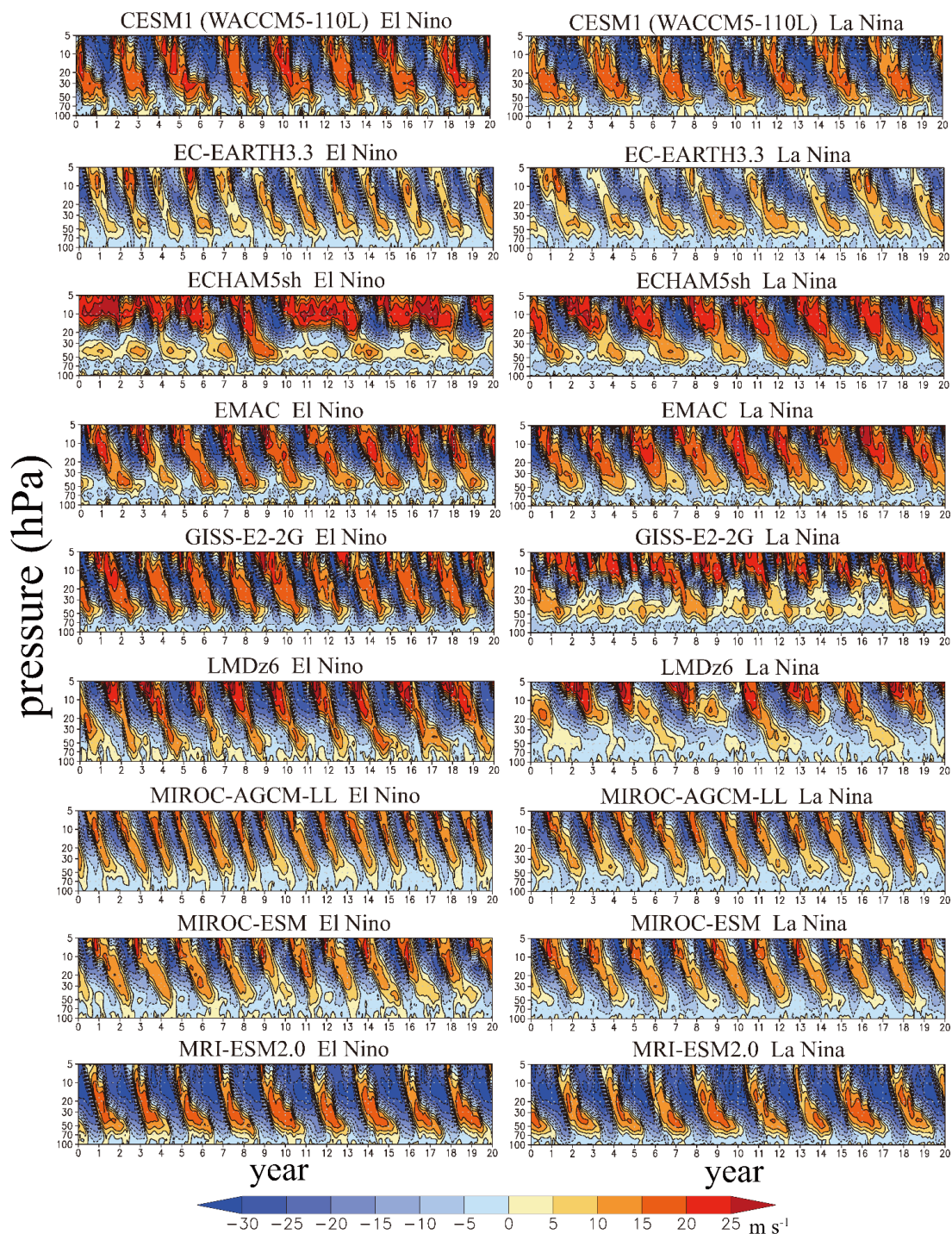
Figure 2: Time-height sections of the monthly mean, zonal mean zonal wind over the equator in the (left) El Niño and (right) La Niña runs with each model. Results from the first 20 years of one ensemble member for each model are shown. Model names are noted above each panel. The contour interval is 5 m s⁻¹.
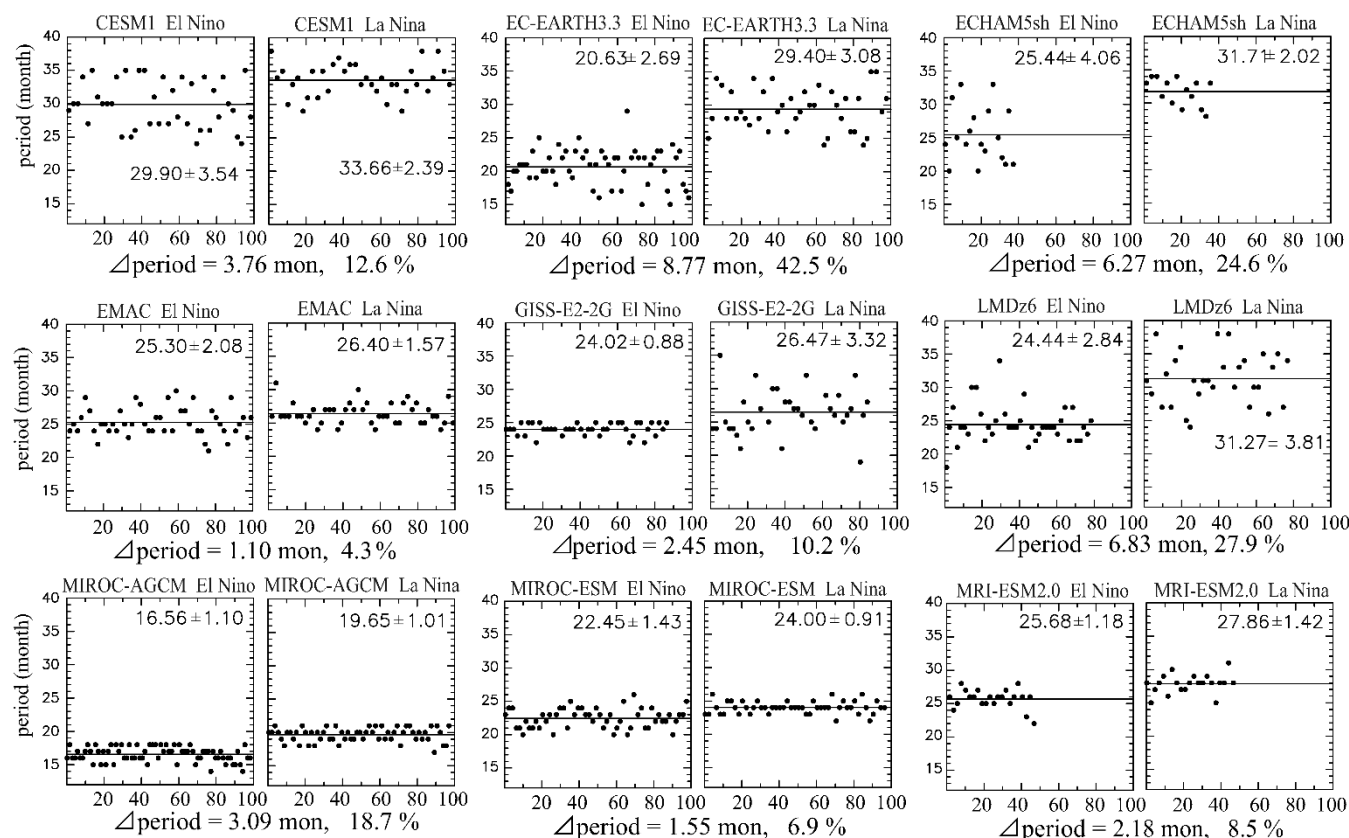
Figure 3: Each pair of panels shows the time series of the QBO periods in the (left) El Niño and (right) La Niña runs for one model. Model names are noted above each panel. Solid horizontal lines show the mean QBO periods. Three ensemble datasets, each spanning 30-years, are used for GISS-E2-2-G model (i.e., the time series is not continuous around 30 and 60 years). One ensemble member is used for other models. Values of mean periods ± one standard deviation are shown within each figure. Differences in the QBO period between La Niña and El Niño, expressed in months, and as a percentage of the La Niña value, are shown at the bottom of each pair figures. Differences of the mean QBO periods between El Niño and La Niña have statistical confidence levels ≥ 99% for all models.

The cycle-to-cycle variability of the simulated QBO periods differs among models. The variability is relatively small in MIROC-AGCM, MIROC-ESM, and MRI. Seasonal locking of the QBO may preferably occur when its period is close to 2-year cycles, such as in GISS during the El Niño run and MIROC-ESM during the La Niña run. Cycle-to-cycle variability differences, evaluated from the standard deviation, are much larger (more than 30% larger) during El Niño in ECHAM, MIROC-ESM, and CESM1, while they are much larger during La Niña in GISS and LMDz, in which the QBO becomes more unstable during La Niña runs, as seen in Fig. 2.

Next, we consider ENSO modulation of QBO amplitude, which is known less robust than that for QBO periods (Serva et al. 2020). Following Dunkerton and Delisi (1985), at each level, we first calculate the standard deviation (σ) of the monthly mean time series after removing the mean seasonal cycle and then estimate the amplitude as $\sqrt{2}\sigma$. Figure 4 shows latitude-height cross-sections of QBO mean amplitude differences between El Niño and La Niña. Colored areas correspond to

315 differences with a statistical confidence level of ≥ 95%, and contours show QBO amplitude in El Niño runs. ECHAM is an outlier model that shows a significantly weaker QBO amplitude during El Niño (i.e., negative differences) throughout the stratosphere, which might result from the unrealistic QBO in the El Niño run, making a simple comparison to other models difficult.
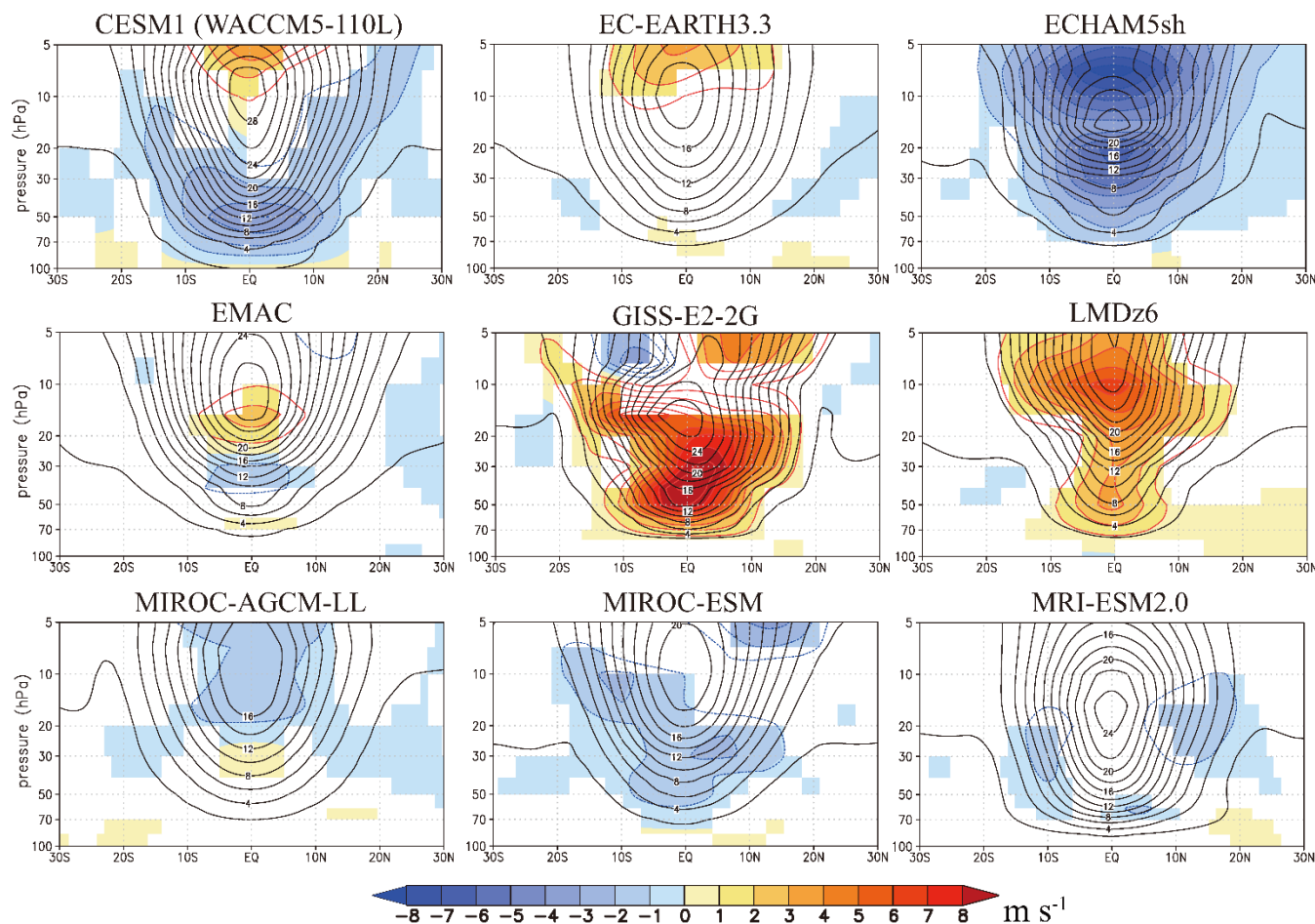
Fig. 4: Contours show the latitude-height cross sections of the mean QBO amplitude in El Niño runs, with intervals of 2 m s⁻¹. The El Niño minus La Niña QBO amplitude differences are shown with colored shading with interval of 1 m s⁻¹. Color shading is shown only where the differences have a statistical confidence ≥ 95%.

Except for ECHAM, the models showing large ENSO differences in QBO amplitude are GISS, LMDz, and CESM1, all of which have variable GWP sources. GISS and LMDz show larger amplitude throughout most of the stratosphere during

325 El Niño compared to La Niña, while CESM1 shows weaker amplitude in the lower stratosphere and larger amplitude above 10 hPa during El Niño. Given that QBO amplitude depends on the zonal phase velocity of gravity waves in addition to wave source strengths, the discrepancy among these three models could be associated with zonal phase velocity differences in resolved and/or parameterized gravity waves. EC-EARTH, EMAC, MIROC-ESM, and MRI, which used fixed GWP sources,

show relatively smaller differences. MIROC-AGCM, in which the QBO is driven only by resolved waves, also shows smaller
330 differences, as shown in Kawatani et al. (2019).

Next, we examine the climatological annual mean differences between the El Niño and La Niña runs. Figure 5 presents a representation of the Walker circulation, namely longitude-height cross-sections of the climatological annual mean, zonal wind at 10°N–10°S for the El Niño run, the La Niña run, and their difference (El Niño minus La Niña). Also shown are the same quantity computed from ERA-I fields composited over El Niño and La Niña periods. These ERA-I results will be 335 discussed first and may be expected to show smaller El Niño minus La Niña differences compared to the QBOi models, since, as mentioned in Section 2, the QBOi simulations imposed SST anomalies scaled by factors of 1.8 and 1.4 for El Niño and La Niña (corresponding to the most intense El Niño and La Niña events). The ERA-I results in Fig. 5 show the expected Walker circulation differences between El Niño and La Niña conditions. Both easterlies in the eastern hemisphere and westerlies in the western hemisphere are stronger in La Niña than in El Niño. Since the Walker circulation filters gravity waves propagating 340 from the troposphere to the stratosphere, a weaker Walker circulation during El Niño could provide more favorable conditions for gravity wave propagation from the troposphere into the stratosphere due to reduced filtering (see Figs. 6 and 7 of Kawatani et al., 2010b). This argument assumes critical-level absorption of otherwise weakly damped, vertically propagating waves, similar to the ideal model of Lindzen and Holton (1968). Over the Pacific, around 120°E–90°W, significantly large easterly differences in El Niño minus La Niña are found from ~500 hPa to 80 hPa, and westerly differences are found below the region 345 with easterly differences. At other longitudes above ~500 hPa, westerly differences are found, associated with smaller easterly differences below.

For both El Niño and La Niña conditions there is some degree of agreement in the Walker circulation in the ERA-I composite and in the QBOi model simulations. However, there is considerable variability in the Walker circulation among the individual model simulations. Most notably, in the ECHAM El Niño runs, the observed easterly jets in the eastern 350 hemisphere are absent, while westerlies in the western hemisphere are much stronger than those in the ERA-I composite. One possible explanation for the unrealistic El Niño QBO simulation in this model, in which westerly phases do not propagate downward (Fig. 2), could be much stronger filtering of eastward waves within the troposphere. During El Niño conditions, the EMAC, GISS, LMDz, and MRI models also show relatively weak easterlies in the eastern hemisphere, while EMAC, GISS, MIROC-ESM, and CESM1 exhibit stronger westerlies in the western hemisphere. During La Niña, all models qualitatively 355 represent one maximum easterly jet around 90°E and two maximum westerly jets around 140°W and 30°W.

Despite variations in the simulated Walker circulation structures between El Niño and La Niña across models, the El Niño minus La Niña difference patterns exhibit remarkable similarity across models and with ERA-I. These results suggest that while the specific El Niño and La Niña circulations may be model-dependent, the ENSO-induced responses in the Walker circulation are well-represented in the QBOi models. All models except CESM1 exhibit stronger easterly differences over the 360 central Pacific compared to westerly differences elsewhere. In CESM1, however, easterly anomalies over the central Pacific are much weaker, while westerly anomalies dominate at other longitudes.

14
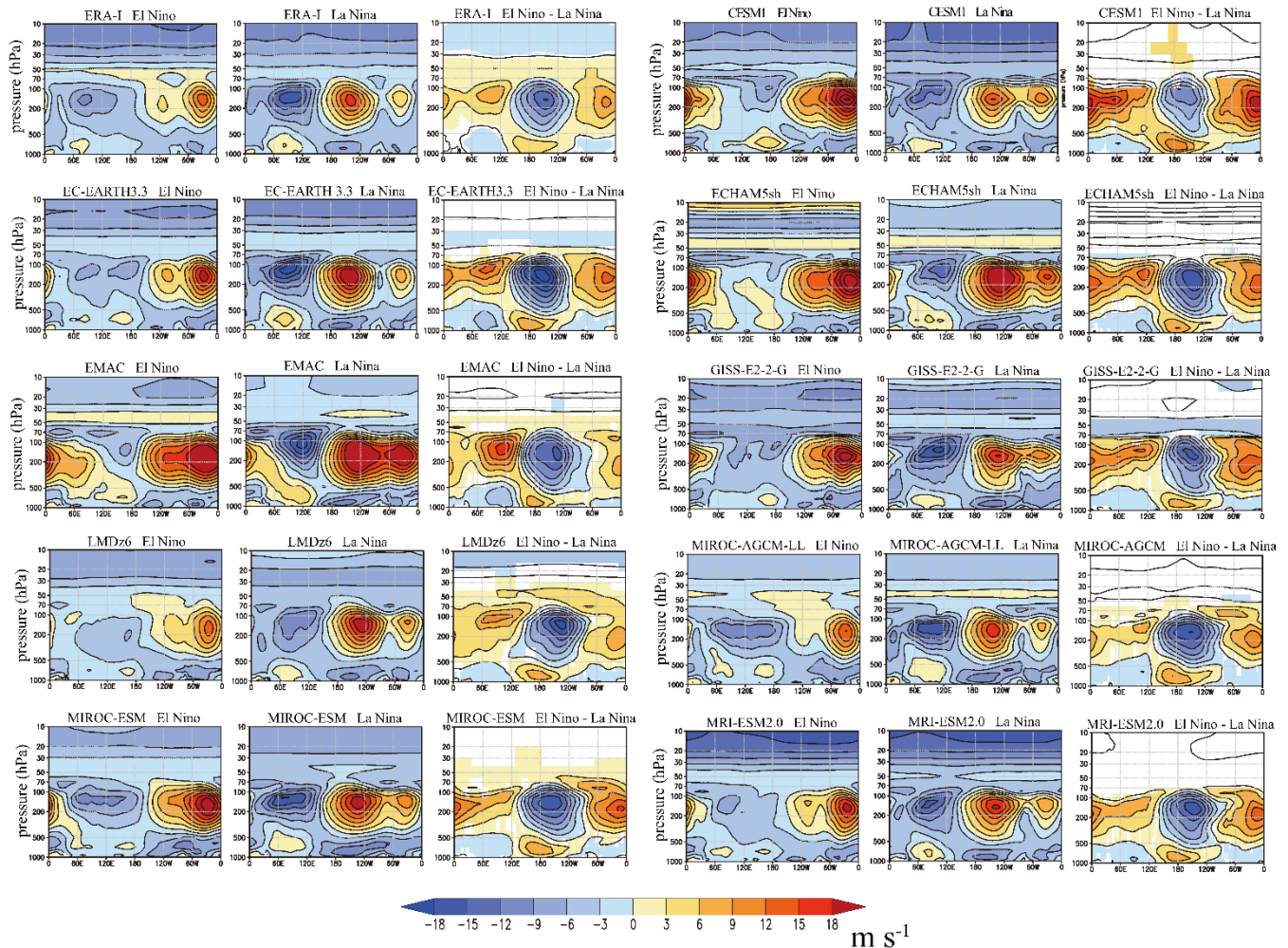
Fig. 5: Each group of three panels shows longitude-height cross sections of the climatological annual mean zonal wind averaged over 10ºN–10ºS during (left) El Niño, (middle) La Niña, and (right) their difference. The top left row of panels shows results for ERA-I observations, and others show results from individual models. For the model results color shading is included where differences are judged to have a statistical confidence ≥ 95%. For the ERA-I observations shading is included where the magnitude of the difference exceeds 1 m s^{-1}.

Figure 6 shows climatological annual mean precipitation differences (El Niño minus La Niña) in CMAP data and in each of the models. Note that ENSO composites of the CMAP data are not multiplied by the arbitrary factors applied to the El Niño and La Niña SST anomalies imposed in the model experiments. All models show positive precipitation differences (note that blue colors correspond to positive values) in the equatorial eastern Pacific and negative precipitation around the Maritime Continent, which are quite similar to those in CMAP. From the central to eastern Pacific a region of slightly reduced precipitation during El Niño conditions extends east to west, north of the equatorial positive differences (a feature clearly largest in MRI and CESM1). Note that this off-equatorial region of negative precipitation differences is related to the southward

15

375   displacement of the ITCZ during El Niño as compared to the northward displacement during La Niña (e.g. Trenberth et al. 1998).
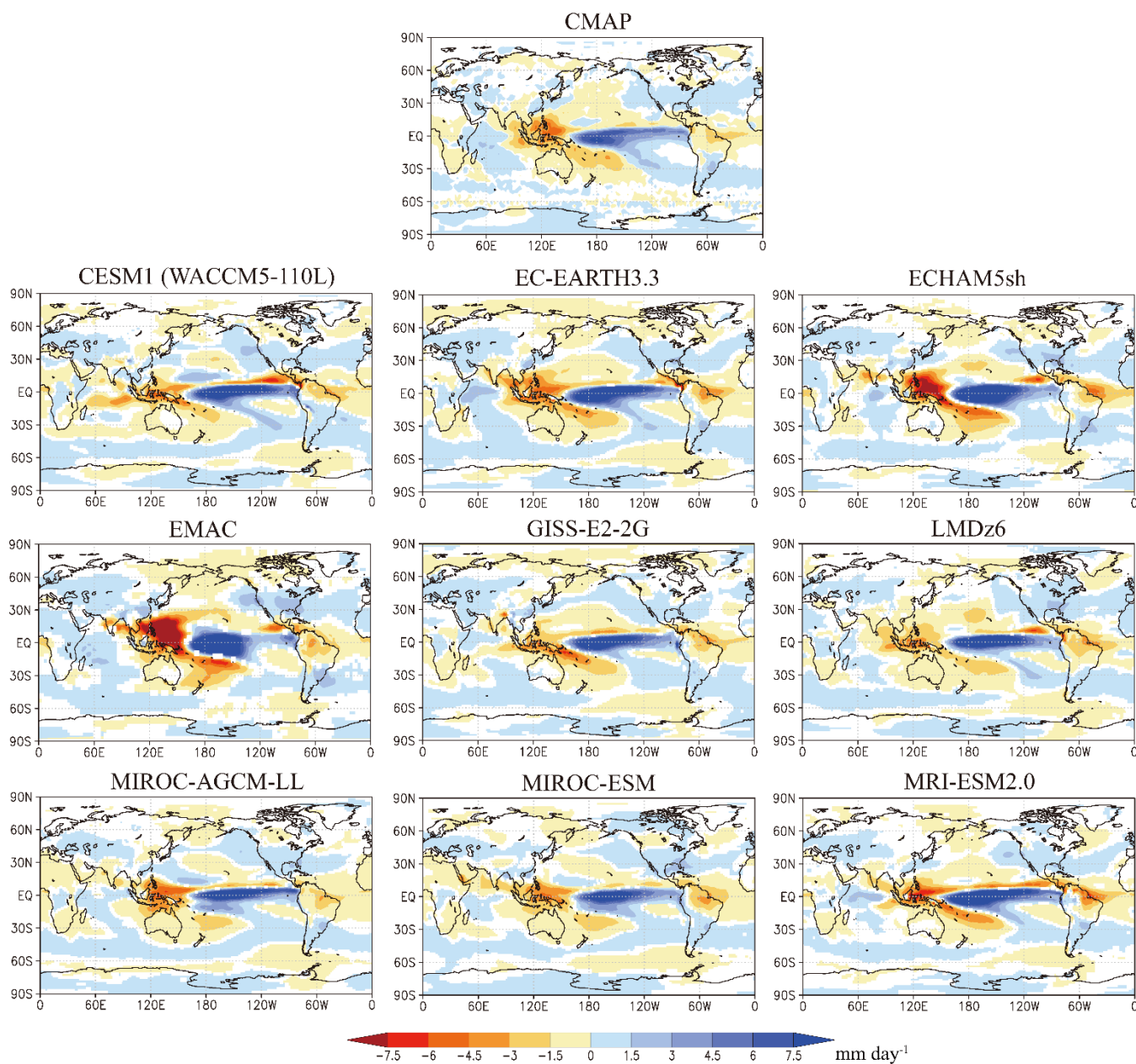
Fig. 6. Climatological annual mean precipitation differences for El Niño minus La Niña conditions for (left-top) CMAP and (others) individual models. Differences with absolute values ≥ 0.1 mm day^{-1} are shaded in CMAP, and those with a statistical confidence ≥
380   **95% are shaded for models.**

        Figures 7a-c present longitudinal variations in El Niño and La Niña mean precipitation and their differences, averaged over 10ºN–10ºS. Longitudinal variations are qualitatively similar between observations and models in both El Niño and La

16

385   Niña runs, although models tend to simulate the precipitation peak to the east of the observed one over the central Pacific in the El Niño run. The longitudinal variations of precipitation differences in 10°S-10°N are also qualitatively similar between CMAP and the models.

    Figure 7d shows latitudinal variations in zonal mean precipitation differences for CMAP and each model. All models simulate larger precipitation during El Niño (i.e., positive differences) over the equator, consistent with observations. Note again that the observed composite here is being compared with model runs forced with amplified El Niño and La Niña SST anomalies. So, for example, the differences in MIROC-AGCM-LL (yellow line) are larger than in CMAP in this experiment,
390   while in the earlier Kawatani et al. (2019) experiments (without amplification of the imposed SST anomalies) the simulated ENSO differences in rainfall agreed well with the CMAP result. Larger precipitation over the equator in El Niño compared to La Niña is a favorable condition for generating equatorially symmetric waves, mostly Kelvin waves.
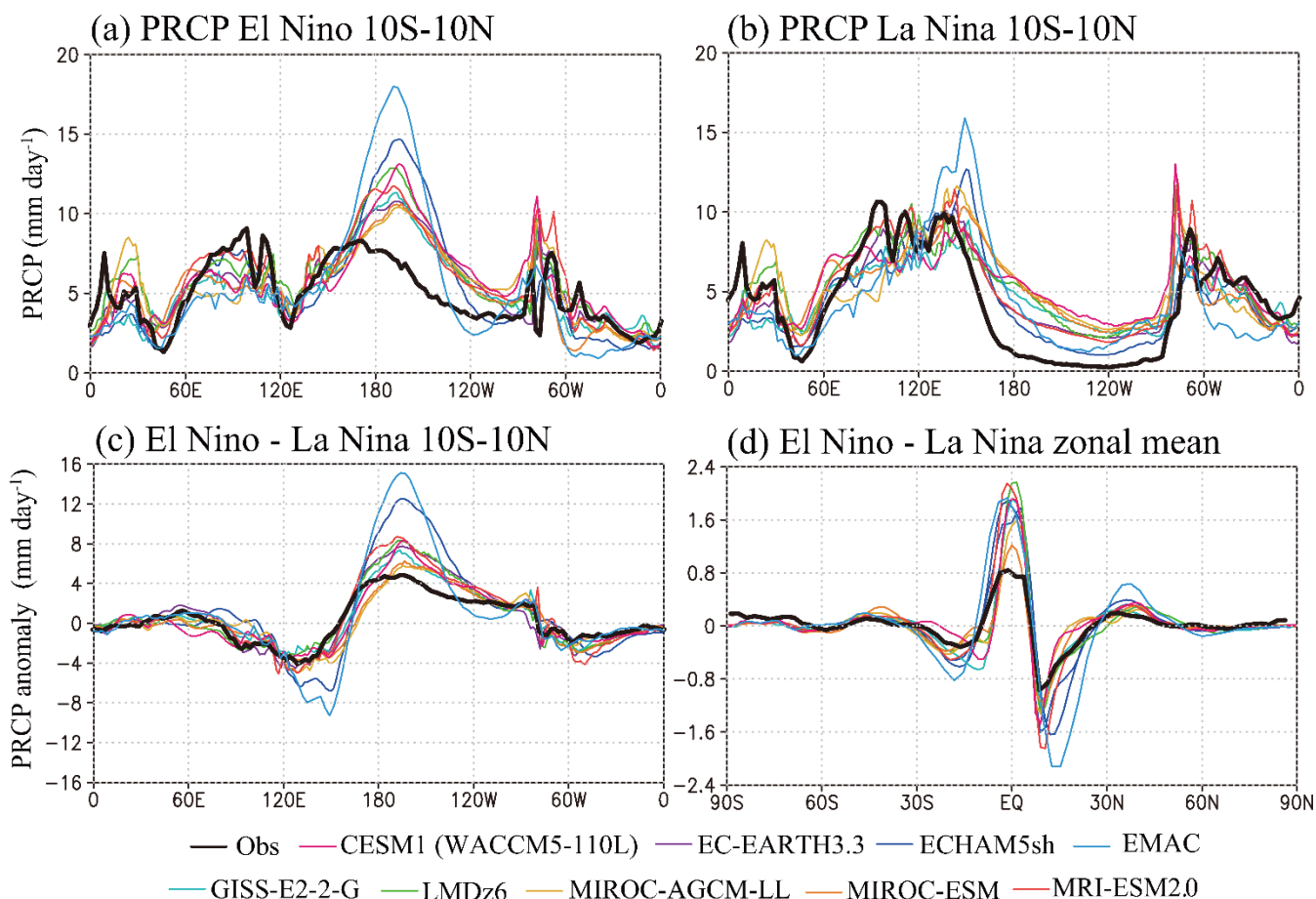

Fig. 7. Longitudinal variations of annual mean precipitation averaged over 10ºN–10ºS in (a) El Niño conditions, (b) La Niña
395   **conditions and (c) their differences. (d) Latitudinal variations of zonal mean El Niño minus La Niña precipitation differences. Black line shows CMAP observations and color lines display results for the individual models.**

17

Figure 8 shows the climatological annual mean, zonal mean temperature in the El Niño (purple lines) and La Niña (green lines) runs, along with their El Niño minus La Niña differences (color) in ERA-I and in the individual models. Over
400 ~30°S–30°N, the troposphere is warmer, and the stratosphere is cooler in El Niño compared to La Niña run (cf. Domeisen et al., 2019) for all the model runs and ERA-I. In both the troposphere and stratosphere, the model El Niño-La Niña differences near the equator tend to be spread somewhat wider meridionally than indicated by ERA-I. In the troposphere, the ERA-I composite displays clearly defined regions poleward of ~30° latitude where the El Niño conditions are cooler than the La Niña conditions, and these regions are not as clear in the model results except for EC-EARTH. One possible reason is the use of
405 extreme ENSO SSTs in the experiments.   In their results using MIROC-AGCM with imposed ENSO SST anomalies based on just more recent ENSOs (and without the extra amplification used in the present study), Kawatani et al (2019; Fig. 7) found these cooler differences, despite not being as cool as ERA-I (see Fig. 7 in Kawatani et al., 2019), but these differences are not found in the present experiment with MIROC-AGCM.

Warm differences in the mid-to-high-latitude stratosphere are found in all models, which are also qualitatively similar
410 to those in ERA-I. However, the vertical and meridional extent of these warm anomalies differ among the models. LMDz shows significantly cooler El Niño-La Niña anomalies in the Southern Hemisphere stratosphere, where MRI and CESM1 simulated significant warm differences. The cooler El Niño-La Niña anomalies in the troposphere around 60°N-90°N in ERA-I are not found in any of the models.

Figure 9 is the same as Fig. 8 but for zonal mean zonal wind. The models successfully reproduce the overall pattern
415 of zonal mean zonal wind El Niño-La Niña differences observed in ERA-I. In the equatorial troposphere, weak westerly differences around 900 hPa and easterly differences around 500–100 hPa are found in both ERA-I and the models, except for CESM1, which simulates smaller easterly differences over the central Pacific and stronger westerly differences at other longitudes (Fig. 5). In the low-to-mid latitudes, the zero contours of the zonal wind are higher in El Niño than in La Niña (see purple and green lines, respectively) in ERA-I, and relatively large westerly differences from the lower troposphere to ~30 hPa
420 are observed outside the equatorial region. All models simulate an upward shift of the zero wind contours in the El Niño run consistent with these westerly differences, but their vertical patterns differ significantly among models. Specifically, significantly deep westerly differences are found up to 5 hPa in GISS, LMDz, and MIROC-ESM. In the poleward regions, weak easterly differences are found from the surface to the stratosphere in ERA-I. These easterly differences also vary among the models, being largest in GISS and smallest in EMAC. LMDz, MRI, and CESM1 also show larger easterly anomalies
425 compared to ERA-I.

Different distributions of the background zonal mean zonal wind could alter wave propagation properties and thus modify the stratospheric Brewer–Dobson circulation (BDC). The westerly El Niño minus La Niña differences in the mid-latitude lower stratosphere are somewhat similar to what is seen in global warming versus present-day climate simulations (e.g., Kawatani et al., 2011).
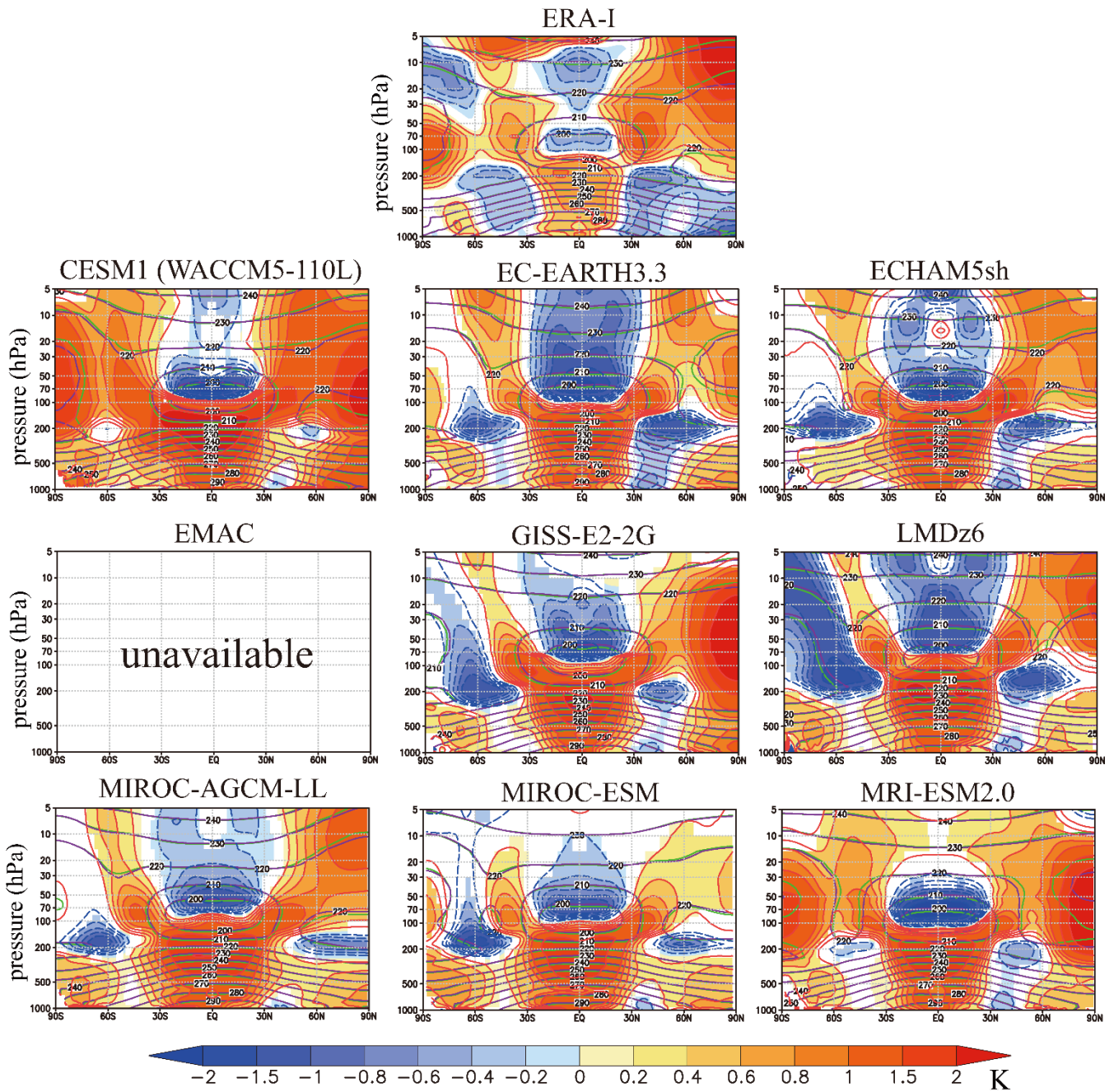
Fig. 8. Contour lines show the climatological annual mean, zonal mean temperature for (purple) El Niño conditions and (green) La Niña conditions for (left top) ERA-I and (others) QBOi models. Contour intervals are 10 K for mean temperature. Color shading included where the magnitude of El Niño minus La Niña differences exceed 0.1 K for ERA-I and where the differences are judged different from zero with statistical confidence ≥ 95% for the model results. Color intervals are ±0.2, 0.4, 0.6, 1, 1.5, and 3 K.
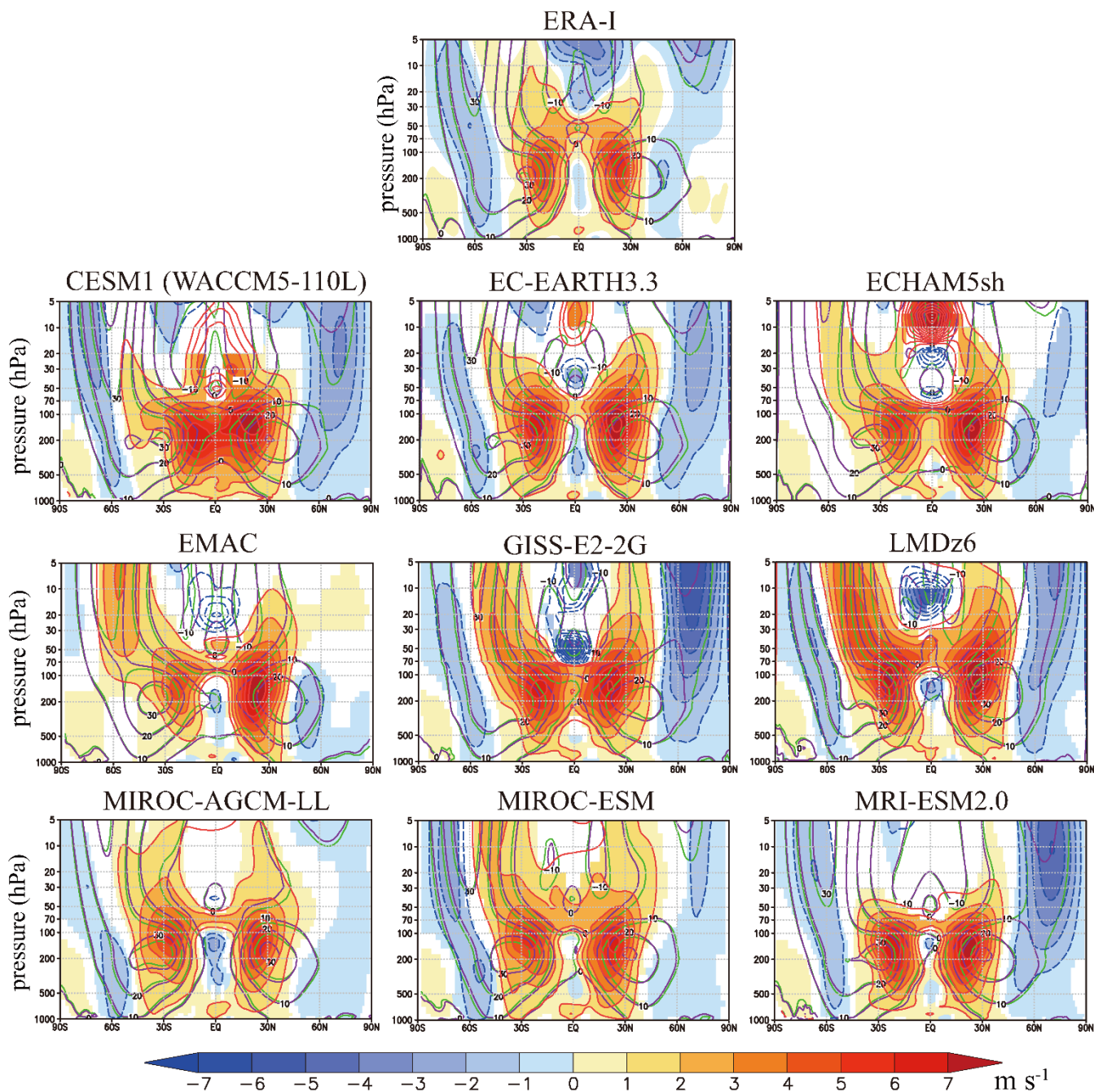
Fig. 9. As in Fig. 8 but for zonal mean zonal wind. Contour intervals are 10 m s⁻¹. Color shading included where the magnitude of El Niño minus La Niña differences exceed 0.2 m s⁻¹ for ERA-I and where the differences are judged different from zero with statistical confidence ≥ 95% for the model results. Color intervals are ±1, 2, 3, 4, 5, 6 and 7 m s⁻¹.

440

4 Contrasting wave forcing and residual mean meridional circulations in El Niño and La Niña from QBOi models

In this section, we discuss the ENSO related effects on the eddy forcing of mean zonal momentum and residual mean meridional circulation in the Transformed Eulerian Mean (TEM) formulation. The mean flow forcing from explicitly resolved eddies as well as GWP are considered. The Eliassen–Palm flux (EP-flux) in spherical and log-pressure coordinates is used (Andrews et al. 1987):

$$F^{(\phi)} = \rho_0 a \cos\phi \left(\bar{u}_z \, \overline{v'\theta'}/\bar{\theta}_z - \overline{u'v'} \right) \tag{1}$$

$$F^{(z)} = \rho_0 a \cos\phi \left\{ \left[f - (a\cos\phi)^{-1}(\bar{u}\cos\phi)_\phi \right] \overline{v'\theta'}/\bar{\theta}_z - \overline{u'w'} \right\} \tag{2}$$

$$\boldsymbol{\nabla} \cdot \boldsymbol{F} = (a\cos\phi)^{-1} \, \partial/\partial\phi \left(F^{(\phi)} \cos\phi \right) + \partial F^{(z)}/\partial z \tag{3}$$

The zonally averaged momentum equation in terms of the TEM formation is expressed as:

$$\bar{u}_t = \bar{v}^* \left[f - (a\cos\phi)^{-1}(\bar{u}\cos\phi)_\phi \right] - \bar{w}^* \bar{u}_z + (\rho_0 a\cos\phi)^{-1} \, \boldsymbol{\nabla} \cdot \boldsymbol{F} + \overline{OGW} + \overline{NOGW} + \bar{X} \tag{4}$$

In the above equations, ρ_0, a, ϕ, z, u, v, w, θ, and f are the (height dependent) mean density, the mean radius of the Earth, latitude, log-pressure height, zonal wind, meridional wind, vertical wind, potential temperature, and Coriolis parameter ($f = 2\Omega \sin\phi$, where Ω is the rotation rate of the Earth), respectively. The subscripts ϕ, z, and t denote the meridional, vertical, and time derivatives, respectively. The mean residual circulations of the meridional and vertical components are expressed by $\bar{v}^*$ and $\bar{w}^*$. Eastward and westward resolved wave forcing of the mean flow correspond to the EP-flux divergence and convergence (i.e., $\boldsymbol{\nabla} \cdot \boldsymbol{F} > 0$ and $\boldsymbol{\nabla} \cdot \boldsymbol{F} < 0$), respectively. $\overline{OGW}$ and $\overline{NOGW}$ are the zonal forcing due to orographic and non-orographic GWP, respectively. The $\bar{X}$ term represents any other unresolved forcing. These variables are not consistently available across all models as shown in Table 2. Therefore, the figures in this section will only present data from models that include these specific variables.

Figure 10 shows the differences between El Niño and La Niña in each model of the annual mean TEM related quantities. Specifically shown are the El Niño-La Niña differences for resolved EP-flux divergence, zonal forcing due to parameterized orographic and to parameterized non-orographic gravity waves, as well as the streamfunction of the residual mean circulation. Also shown as black contour lines in the left three columns are the zonal mean zonal wind in each El Niño run. Positive wave forcing values correspond to stronger eastward wave driving of the mean flow, while negative values indicate stronger westward driving in El Niño compared to La Niña. Note also that positive and negative residual mean circulation streamfunction values represent clockwise and counterclockwise circulations, respectively.

First, we focus on results from the MIROC-AGCM-LL, which was also used in the Kawatani et al. (2019) study (but with more moderate imposed ENSO SST anomalies, as explained in the previous section). Figure 8 of Kawatani et al. (2019) showed the EP flux vectors in El Niño and La Niña simulations. Notably this showed that resolved waves transporting westward mean momentum propagate upward around 30°N–70°N and 30°S–70°S and also propagate equatorward in low latitudes in the El Niño run. This equatorward propagation weakens considerably around the zero lines of the mean zonal wind. There is also strong westward wave forcing due to orographic GWP in the mid-latitude upper-troposphere and lower-

stratosphere (UTLS) region in both hemispheres, where westerlies are weak. This presumably plays a substantial role in

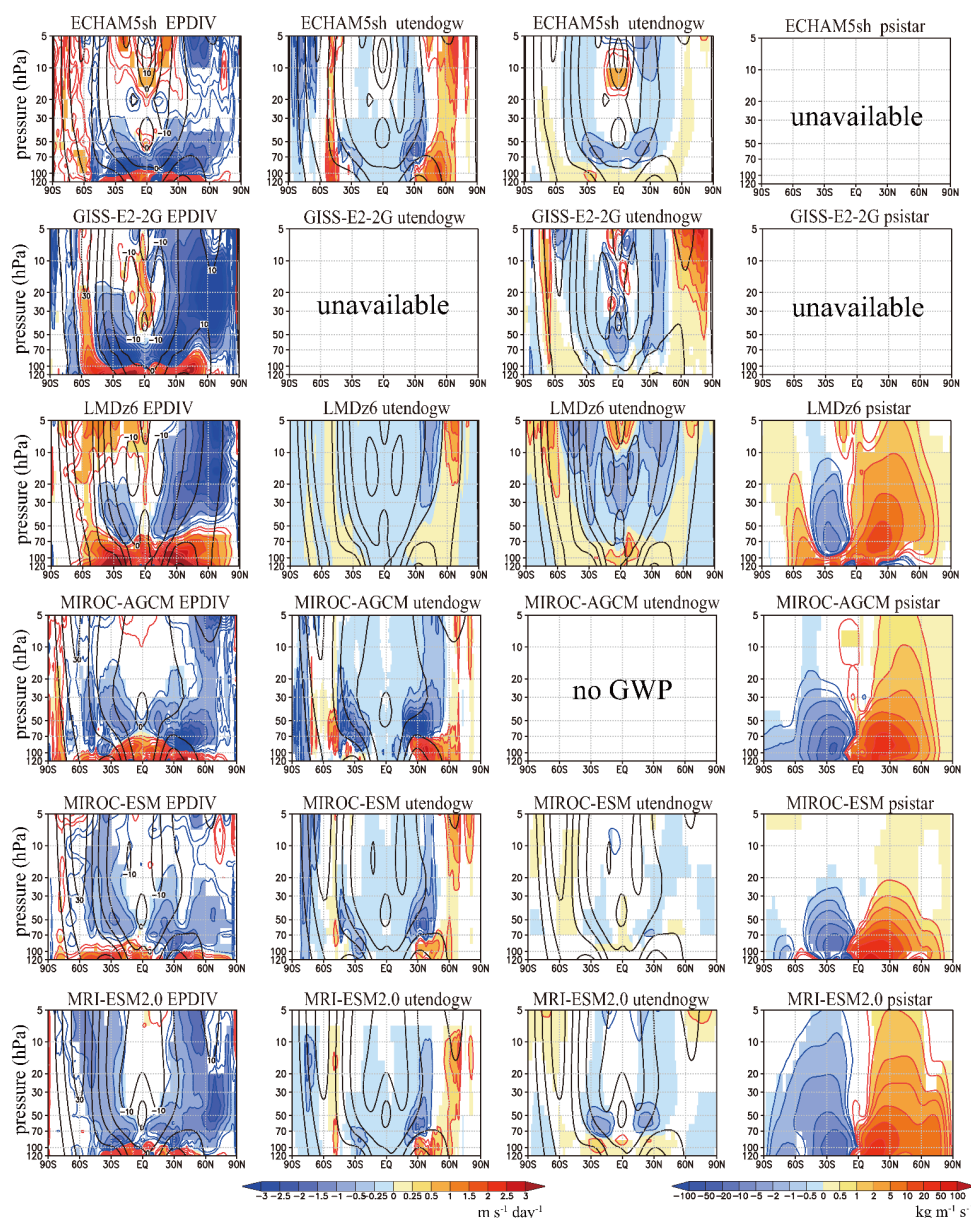475 decelerating the upper part of the subtropical westerly jet.

Fig. 10. The color shading shows El Niño minus La Niña c annual mean differences of: (left column) EP-flux divergence, and zonal momentum forcing due to (2nd column) orographic and (3rd column) non-orographic GWP, and (4th column) residual mean circulation streamfunction. For the first 3 columns the mean zonal wind is contoured with intervals of 10 m s⁻¹. Color intervals are

480 **at ±0.25, ±0.5, ±1.0, ±1.5, ±2.0, ±2.5, and ±3.0 m s⁻¹ day⁻¹ for the first 3 columns and ±0.5, ±1.0, ±2.0, ±5.0, ±10, ±20, ±50, and ±100 kg m⁻¹ s⁻¹ for the 4th columns. Color shading is included only where differences in El Niño minus La Niña values are statistically significant at a confidence level ≥ 95%.**

22

These characteristics of the EP flux vectors are very similar to those found in the present MIROC-AGCM experiments (not shown). The El Niño-La Niña differences in EP-flux divergence seen in the present Fig. 10 (and the earlier Kawatani et al., 2019, Figure 8) features strong westward forcing above ~70-100 hPa and eastward forcing below these levels, showing that more resolved waves transporting westward momentum preferentially propagate into the lower stratosphere during El Niño. This is consistent with the upward shift of zero lines of zonal wind in El Niño compared to La Niña (see purple and green contours in Fig. 9). Westward forcing differences due to orographic GWP occur in the mid-latitudes around 30–80 hPa in both the Northern and Southern Hemispheres, whereas eastward forcing anomalies are seen below the westward forcing anomalies, particularly in the Northern Hemisphere. Kawatani et al. (2019) noted that surface winds over major mid-latitude mountain regions change very little between the El Niño and La Niña simulations, and the change in orographic GWP may be mainly due to altered mean flow filtering. Shifting the zero line of the zonal wind also allows deeper penetration of orographic waves and spreads the westward forcing from the waves to higher altitudes.

The overall characteristics of resolved wave forcing and orographic GWP differences in the off-equatorial UTLS region are qualitatively similar among models, except orographic GWP in LMDz. In GISS, LMDz, and MRI, relatively large westward forcing anomalies by resolved waves extending from the lower to the upper stratosphere coincide with large easterly mean wind differences around 60°N (Fig. 9). Differences in non-orographic GWP show somewhat similar distributions among ECHAM, MIROC-ESM, and MRI, which include the Hines-type GWP, while GISS and LMDz, which both use variable sources in their GWP, show different structures.

The residual mean circulation differences (4th column) show positive and negative anomalies in the Northern Hemisphere and Southern Hemisphere, respectively. Consistent with wave forcing differences by both resolved and parameterized waves, MIROC-AGCM and MIROC-ESM show that differences of the residual mean circulation are mainly found in the shallow branch of the BDC, while LMDz and MRI show larger differences, that extend to the deep branch of the BDC.

To investigate the mean ascent in the equatorial lower stratosphere, we analyzed the residual vertical velocity in the TEM formation defined as:

$$\overline{w}^* = \overline{w} + (a\cos\phi)^{-1}\left(\cos\phi\,\overline{v'\theta'}/\overline{\theta}_z\right)_\phi \tag{5}$$

Figure 11 shows the vertical profiles of El Niño $\overline{w}^*$, La Niña $\overline{w}^*$, El Niño minus La Niña differences, and the ratio of El Niño to La Niña (i.e., El Niño divided by La Niña), averaged over 20°S–20°N for each model. All models simulate a minimum $\overline{w}^*$ near 50 hPa in both El Niño and La Niña simulations. However, the magnitude of this minimum varies considerably, ranging from approximately 0.2 mm s^{-1} in MIROC-AGCM to approximately 0.4 mm s^{-1} in LMDz.

All models simulate stronger equatorial tropical upwelling in El Niño compared to La Niña up to ~10 hPa. Specifically, large differences are found around 100-50 hPa, ranging from 0.06 mm s^{-1} (MIROC-ESM) to 0.15 mm s^{-1} (GISS) in terms of raw differences (Fig. 11c), and ~22% (LMDz) to 40% (EC-EARTH) in terms of fractional change between the El Niño and

515 La Niña runs. In the middle to upper stratosphere the $\overline{w}^*$ differences become smaller, but LMDz and MRI show relatively

large differences associated with the ENSO related modulation that extends to the deep branch of the BDC (Fig. 10).
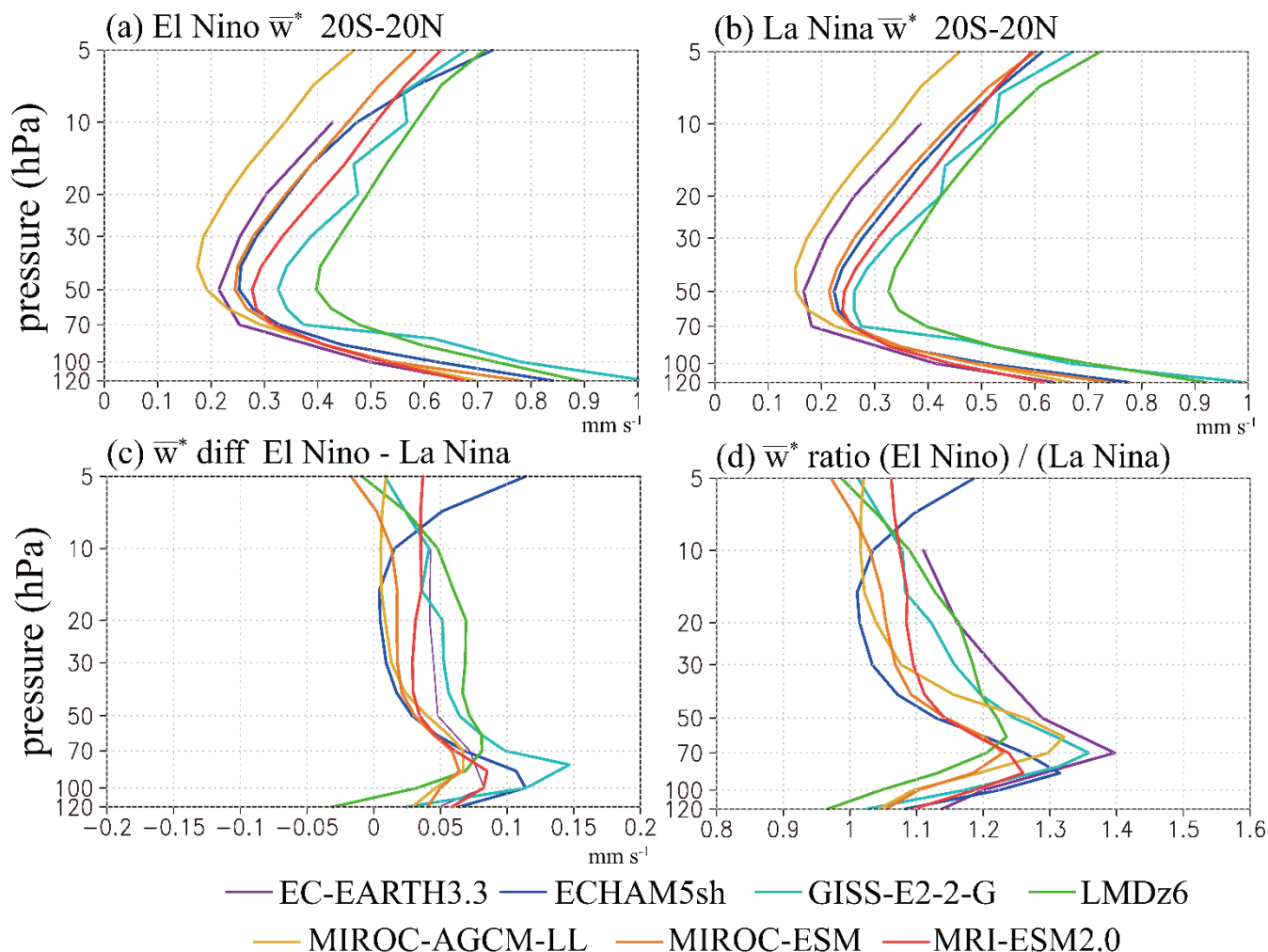

Fig.11. Model simulated vertical profiles of residual vertical velocity averaged over 20°S-20°N in (a) El Niño experiment, (b) La Niña experiment, (c) El Niño minus La Niña values and (d) ratio of El Niño to La Niña values. The units for panels (a-c) are mm s^{-1}.

520   If wave forcing relevant to the QBO remains constant, $\overline{w}^*$ could be the primary determinant of the QBO period

(Dunkerton, 1997). The increase in equatorial $\overline{w}^*$ during El Niño runs, by itself, is expected to lead to a lengthening of the

QBO period. However, the specific altitudes at which $\overline{w}^*$ changes would most strongly   influence the overall QBO period

remain unclear. Notably, in any event our results demonstrate significantly shorter QBO periods in El Niño simulations (Fig.

3), which is opposite of what would be expected simply from an intensification of the mean upwelling. Presumably the effects

525 of the ENSO related changes in the wave driving of the QBO must be considered.

Next, we examine differences in parameterized wave fluxes between El Niño and La Niña. Relevant results are summarized in Fig. 12 by 4 panels for each model. The upper two panels for each model in Fig. 12 are 100 hPa horizontal maps showing both the absolute values of parameterized non-orographic gravity wave momentum flux during El Niño (contours), as well as the differences between El Niño and La Niña (color shading). Results are shown separately for the

530   eastward and westward propagating parameterized gravity waves (left and right panels, respectively). The lower panels present the longitudinal variations of the absolute values of eastward and westward 100 hPa momentum fluxes averaged over 10°S-10°N during El Niño and La Niña. Datasets from only four models: ECHAM, MIROC-ESM, MRI-ESM, and CESM1, provide these variables (see Table 2). Note again that ECHAM, MIROC-ESM, and MRI-ESM used Hines-type non-orographic GWP, with fixed sources of parameterized gravity waves, but wave fluxes are modulated by filtering effects of background winds

535   above the launched level. CESM1 utilized variable parameterized gravity wave sources, related to convective heating.

The Walker circulation plays a significant role in filtering gravity waves propagating from the troposphere to the stratosphere (e.g., Kawatani et al., 2009, 2010b). Eastward propagating gravity waves are preferentially filtered by background eastward winds (i.e., westerlies), and westward waves by westward winds (i.e., easterlies). The Walker circulation in the middle to upper troposphere is easterly in the eastern hemisphere and westerly in the western hemisphere (Fig. 5), creating

540   favorable conditions for eastward waves propagating upward in the eastern hemisphere and for westward waves in the western hemisphere.

In ECHAM, MIROC-ESM, and MRI-ESM, eastward fluxes during El Niño reach a maximum near the equator from ~30°E to ~120°W, while westward fluxes are at their minimum over the equator at these longitudes (see contour lines in Fig. 12). This finding corresponds well with the middle to upper tropospheric easterlies associated with the Walker circulation

545   during El Niño (see the leftmost panel in each model in Fig. 5).

Longitudinal variations in eastward and westward fluxes (see the lower panels for each model in Fig. 12) are qualitatively similar across these three models for both El Niño and La Niña. Eastward fluxes are weaker from ~0°E to ~150°E and stronger from ~150°E to ~120°W during El Niño compared to La Niña. Conversely, westward fluxes are weaker from ~140°E to ~110°W and stronger at other longitudes during El Niño compared to La Niña. Consequently, differences in

550   eastward fluxes (El Niño minus La Niña; see colors in the upper panels) are particularly large and positive around the central Pacific, associated with negative anomalies to the east and west. In contrast, differences in westward fluxes are largely negative around the central Pacific. These characteristics are well correlated with background zonal wind differences associated with the Walker circulation (Fig. 5) in these three models (which all use Hines-type GWP).

The distribution of parameterized gravity wave fluxes in CESM1, and their differences between El Niño and La Niña,

555   differ from other models and exhibit more locally distinct structures. This should be because non-orographic gravity wave sources in CESM1 are related to parameterized convective heating. Differences in wave fluxes seen at 100 hPa are a result of both variable wave sources and filtering caused by the Walker circulation. During El Niño, eastward fluxes peak around the central Pacific, associated with maximum precipitation (compare Fig. 7a with the red lines in the lower panels of Fig. 12). In contrast, maximum westward fluxes shift to the eastern Pacific. During La Niña, the maximum of both eastward and westward

560 fluxes shifts to the western Pacific, corresponding to the precipitation shift (compare Fig. 7b with the blue lines in the lower
panels of Fig. 12).
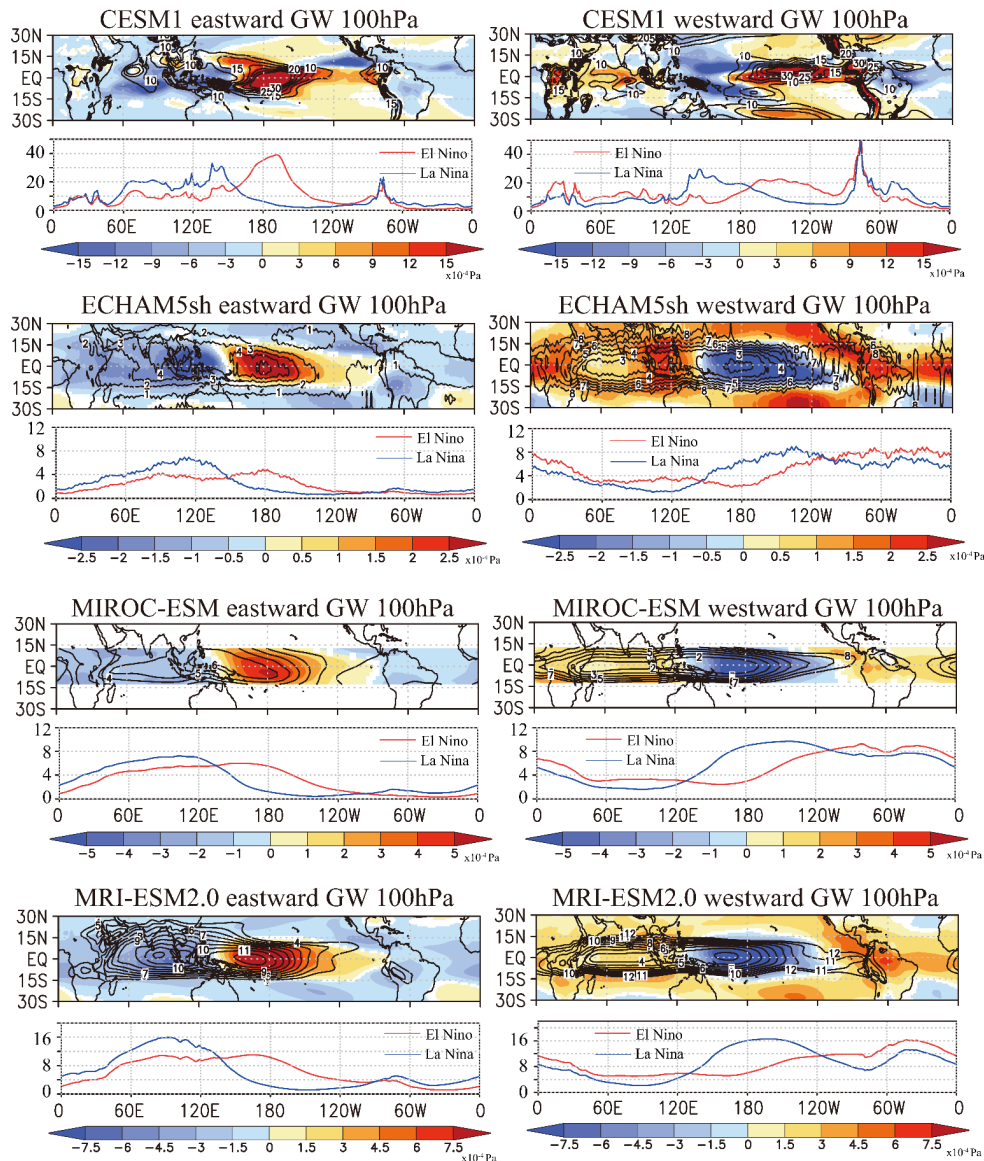
Fig.12. Results for the parameterized non-orographic gravity wave 100 hPa fluxes of zonal momentum in four individual models. The left (right) columns are for eastward (westward) waves. The upper panels for each model are maps showing the absolute value
565 **of the fluxes in the El Niño experiment (contours) and the El Niño minus La Niña value (color shading). Contour intervals are 1×10^{-5} (Pa) except WACCM which are 5×10^{-5} (Pa). Color intervals are 0.5, 1, 1.5 and 3×10^{-5} (Pa) for ECHAM5sh, MIROC-ESM, MRI-ESM2.0 and WACCM, respectively, and color shading is shown only where the difference is significant with statistical confidence $\geq$ 95%. The lower panels of each model show the longitudinal dependence of wave fluxes averaged over 10°S-10°N in (red) El Niño and (blue) La Niña experiments. Note that the vertical axis scales differ among the panels.**

570   The El Niño minus La Niña differences in eastward fluxes show positive values from the central to east Pacific (see colors in the upper panels of Fig. 12), where maximum easterly anomalies of the Walker circulation are located (Fig. 5). Negative values correspond to areas of westerly anomalies of the mid-to-upper tropospheric Walker circulation at other longitudes. These differences are somewhat similar to those found in ECHAM, MIROC-ESM, and MRI. In contrast to eastward waves, differences in westward fluxes in CESM1 have large positive values in the eastern Pacific associated with

575   positive precipitation anomalies (see Fig. 6). V-shaped negative anomalies are found around 150°E, also associated with negative precipitation anomalies. In CESM1, as well as in other models, the point of confluence between the Intertropical Convergence Zone (ITCZ) and the South Pacific Convergence Zone (SPCZ) shifts westward during La Niña compared to El Niño, consistent with observations (not shown).

    While output data of parameterized gravity wave fluxes in LMDz were not available at the time of this analysis, this

580   model, which also uses variable parameterized wave sources related to precipitation activity, showed similar structures affected by precipitation distributions (Dr. Lott, personal communication). Variable sources of parameterized non-orographic gravity wave fluxes in the equatorial region likely have a significant influence on both precipitation and Walker circulations, potentially impacting the representation of the QBO. A detailed investigation of the three-dimensional distributions of parameterized wave fluxes modulated by ENSO, including model dependence, would be of interest and remains a topic for

585   future research.

    Next, we discuss wave forcing of the mean flow in QBO composite cycles for El Niño and La Niña runs. The composite was defined based on the phase of the zonal wind QBO. Month zero of the composite is taken to be when the zonal mean wind at 20 hPa in the deseasonalized and smoothed (5-month running mean) zonal wind series changes from westerly to easterly (Kawatani et al. 2019). Composite values of the original unsmoothed data were then computed for ±18 months

590   around these zero months. Figure 13 shows composited zonal mean zonal wind, zonal wave forcing due to resolved waves (i.e., EP flux divergences) and parameterized non-orographic GWP in 10°S-10°N during El Niño and La Niña. Note that these composite fields are meridionally averaged from 10°N to 10°S, and thus the structure of the QBO is somewhat different compared with that just over the equator (Fig. 2).

    As shown in Fig. 2, the ECHAM QBO during El Niño is somewhat unrealistic (see contour lines), and the structure

595   of the composite QBO does not show continuous downward propagation with weakening amplitude (i.e., westerly QBO has two maxima around 40 hPa and 7 hPa), although a more realistic QBO is found during La Niña. These differences are related to those of QBO amplitude (Fig. 4), in which only ECHAM shows large negative ENSO differences (i.e., El Niño amplitude is weaker) throughout the stratosphere with two minima at ~30 hPa and ~7 hPa. Zonal wave forcing due to both resolved and parameterized waves is larger during La Niña than El Niño at 10-40 hPa. ECHAM is the only model in which wave forcing

600   during La Niña is larger than El Niño at these altitudes. Since zonal wave forcing distribution is closely related to the vertical shear of the zonal wind as well as wave source strength, it is difficult to compare the results of this model to others based its QBO response to El Niño.
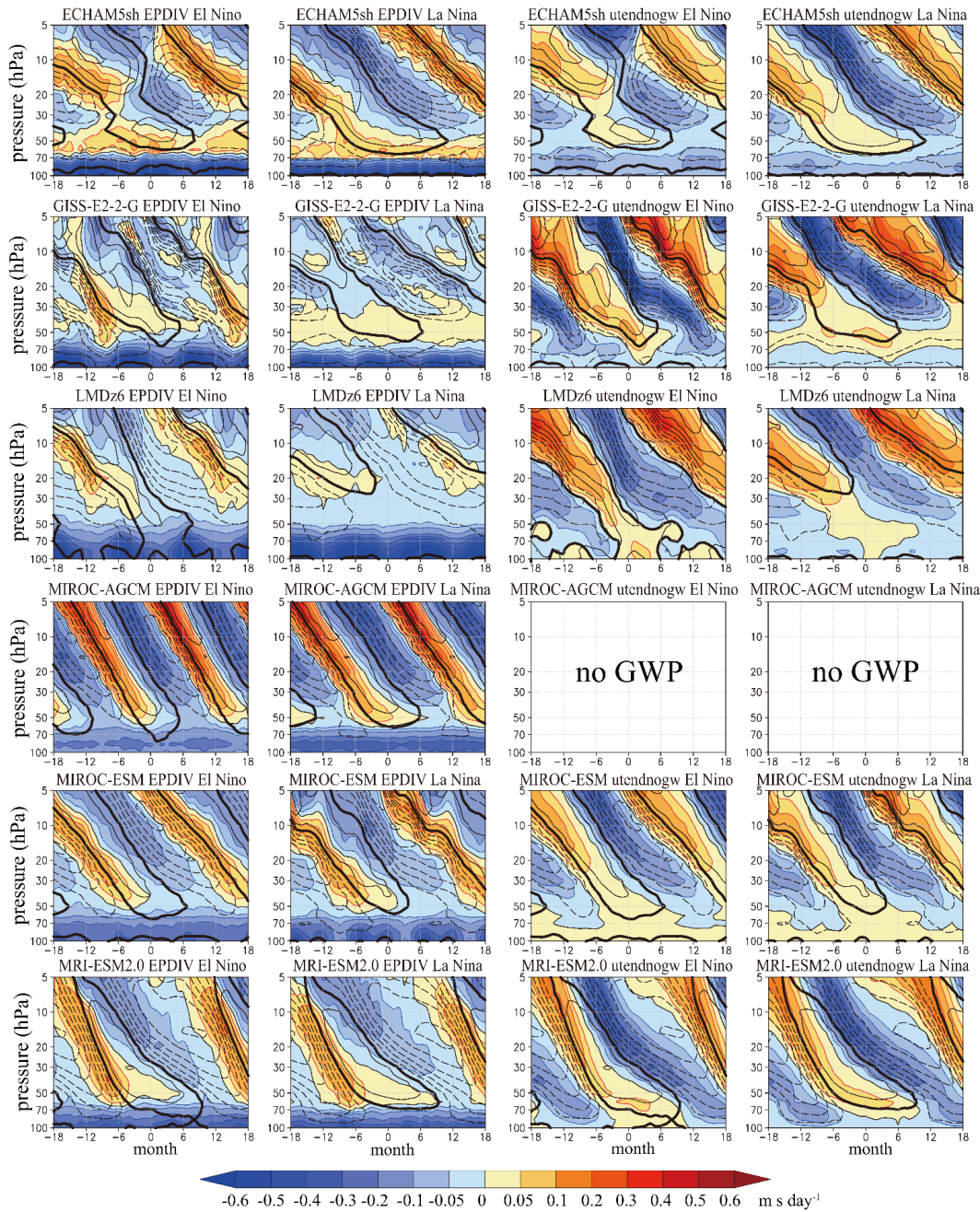
Fig. 13: The contours in each panel show the QBO cycle composites of the zonal mean zonal wind averaged over 10°S–10°N for one model in either El Niño (columns 1 and 3) or La Niña (columns 2 and 4) experiments. The color shading in columns 1 and 2 shows the EP flux divergence from resolved motions averaged over 10°S–10°N. The color shading in columns 3 and 4 shows the mean flow forcing from the non-orographic gravity wave drag parameterizations also averaged over 10°S–10°N. The QBO composite in each case is made relative to month zero which corresponds to the westerly-to-easterly phase transition of the zonal wind at 20 hPa. The contour interval is 5 m s⁻¹. The color intervals are ±0.05, 0.1, 0.15, 0.2, 0.3, 0.4, and 0.5 m s⁻¹ day⁻¹.

605

610   The GISS and LMDz models, which both use variable sources of parameterized GWP, produce similar behavior in their simulations of the QBO. For both models the descent of the westerly phase of the QBO into the lower stratosphere is more evident during El Niño compared to La Niña. As seen in Fig. 4, the QBO amplitude in both models is larger from ~70 hPa to ~10 hPa during El Niño. Both models show larger eastward forcing due to resolved waves during El Niño, specifically around 20-50 hPa in GISS and 10-30 hPa in LMDz. As seen in Fig. 7d, precipitation over the equator is significantly larger
615   during El Niño than La Niña, which is a favorable condition to generate Kelvin waves, which can contribute to driving the westerly phase of the QBO (e.g., Kawatani et al. 2010, 2019). In a forthcoming companion paper (which is core paper 3 of the QBOi-ENSO project as discussed in Section 1 above) Elsburly et al. (personal communication), illustrated that convectively coupled Kelvin waves are more active in El Niño than La Niña runs. Other characteristics for these two models are that zonal wave forcing by parameterized waves is much larger than that by resolved waves in both eastward and westward accelerations.
620   In addition, parameterized wave forcing below is stronger during El Niño than La Niña for both eastward and westward directions, especially below 30 hPa.

On the other hand, in MIROC-ESM and MRI, differences in resolved and parameterized wave forcing are not as large as those in GISS and LMDz. In MRI, westward forcing by parameterized waves is generally larger than that by resolved waves, especially in the lower stratosphere. This is consistent with previous studies (e.g., Giorgetta et al. 2002), as the easterly phases of the QBO are mainly driven by small-scale gravity waves (e.g., Kawatani et al. 2010). In the MIROC-ESM, parameterized
625   eastward wave forcing is significantly smaller than that from resolved waves at 30-50 hPa.

In MIROC-AGCM, in which the QBO is driven by resolved waves only, asymmetry of wave forcing between El Niño and La Niña is found below ~40 hPa for westward forcing. Kawatani et al. (2019) show that these differences are mainly due to gravity waves with zonal wavenumbers greater than 42, i.e., smaller-scale gravity waves that could not be resolved by
630   a moderate resolution T42 model. In this model the mean QBO period difference between El Niño and La Niña is ~3 months (Fig. 3), which makes only modest differences in the composite. However, the slightly delayed downward phase progression of the easterly regime around 30-50 hPa in La Niña relative to El Niño seen earlier in Fig. 2 is also found in these composites (see the contour lines around 30–50 hPa during months 3–9 in Fig. 13).

Figure 14 presents vertical profiles of mean eastward and westward forcing due to resolved and parameterized waves
635   during El Niño and La Niña averaged over 10°S-10°N. For simplicity, the mean eastward and westward wave forcing at a specific altitude was calculated by summing the forcing when the sign was positive and negative for all periods in each model, respectively, and then averaging the results. Here, resolved, parameterized, and total (i.e., resolved plus parameterized) wave forcing is shown separately during El Niño and La Niña.

As discussed for Fig. 14, ECHAM is the only model which shows significantly larger total wave forcing during La
640   Niña (black dashed lines) compared to El Niño (black solid lines) at most altitudes between 70-5 hPa as also seen in Fig. 14, but we do not discuss this further due to unrealistic structures of the QBO during El Niño in this model. In GISS and LMDz, we confirm again that parameterized wave forcing (red lines) is generally much larger than resolved wave forcing (blue lines), especially above ~30 hPa (note that exact altitudes of positive or negative differences depend on eastward or westward forcing

as well as the model). Total wave forcing is larger during El Niño below ~20 hPa in both eastward and westward directions in

645 GISS, and is larger at all altitudes for eastward waves during El Niño and up to ~15 hPa for westward waves in LMDz.

In MIROC-ESM, eastward wave forcing by resolved waves is larger than parameterized waves, while westward wave forcing due to resolved and parameterized waves is comparable above ~40 hPa. Differences in total wave forcing in this model are almost identical between El Niño and La Niña, except for slightly larger westward forcing in El Niño at 40-70 hPa. In the MRI, total eastward wave forcing in El Niño is significantly larger above 20 hPa, which is mainly due to differences in resolved

650 wave forcing between El Niño and La Niña. For westward waves, parameterized wave forcing is much larger than resolved wave forcing. Differences in total wave forcing are found below 40 hPa, with larger forcing during El Niño. In MIROC-AGCM, both eastward and westward resolved wave forcing is larger during El Niño than La Niña, with particularly clear differences found above 40 hPa for eastward and 40-60 hPa for westward waves.

Finally, we briefly discuss the QBO period modulation associated with differences in tropical upwelling and wave

655 forcing, except for ECHAM for the reasons mentioned above. All models consistently simulate longer QBO periods during La Niña than El Niño. Both GISS and LMDz, which utilize variable sources of parameterized GWP, exhibit distinctly larger wave forcing during El Niño, despite having quantitatively different vertical profiles of this forcing (Fig. 14). Tropical upwelling $\overline{w}^*$ differences are larger in GISS compared to LMDz up to ~50 hPa but are smaller above this level (i.e., LMDz simulate stronger $\overline{w}^*$, see Fig. 11). The QBO period is 10.2% longer during La Niña in GISS and 27.9% longer in LMDz (Fig. 3),

660 indicating LMDz shows a much stronger ENSO effect on the simulated modulation of QBO period. As seen in Fig. 2, the GISS QBO in the La Niña run shows continuous westerly around 50 hPa, while downward propagation of QBO westerly phases sometimes stalls around 20 hPa in LMDz. These different QBO modulations make it difficult to simply judge wave forcing and $\overline{w}^*$ differences to evaluate the factors responsible for the distinct QBO period differences between the two models.

MIROC-ESM and MRI, which utilize Hines-type GWP with fixed wave sources, exhibit smaller differences in wave

665 forcing. Notably, these two models demonstrate the least modulation of the QBO period in association with ENSO, with variations of 6.9% and 8.5% for MIROC-ESM and MRI respectively (Fig. 3). MIROC-AGCM shows larger resolved wave forcing during El Niño than La Niña, although the differences are not very large and QBO period modulation by ENSO is 18.7%. We cannot definitively conclude that models with variable GWP sources generally have a simulated period that is more sensitive to ENSO modulation than those with fixed sources. Indeed, some models with fixed GWP sources, such as EC-

670 EARTH, and some with variable sources, such as CESM1, exhibit substantial modulations, suggesting that other factors beyond the variability of the GWP source are also important. Further investigation of these models is hampered by the incomplete model variables in the available data sets.

This simple analysis with limited model output data cannot fully explain quantitative differences in QBO periods between El Niño and La Niña. More detailed wave analyses, based on TEM diagnostics using high temporal datasets, zonal

675 wavenumber versus frequency spectra of EP-flux and precipitation, parameterized wave forcing properties including their 3-dimensional variations, etc., are required.
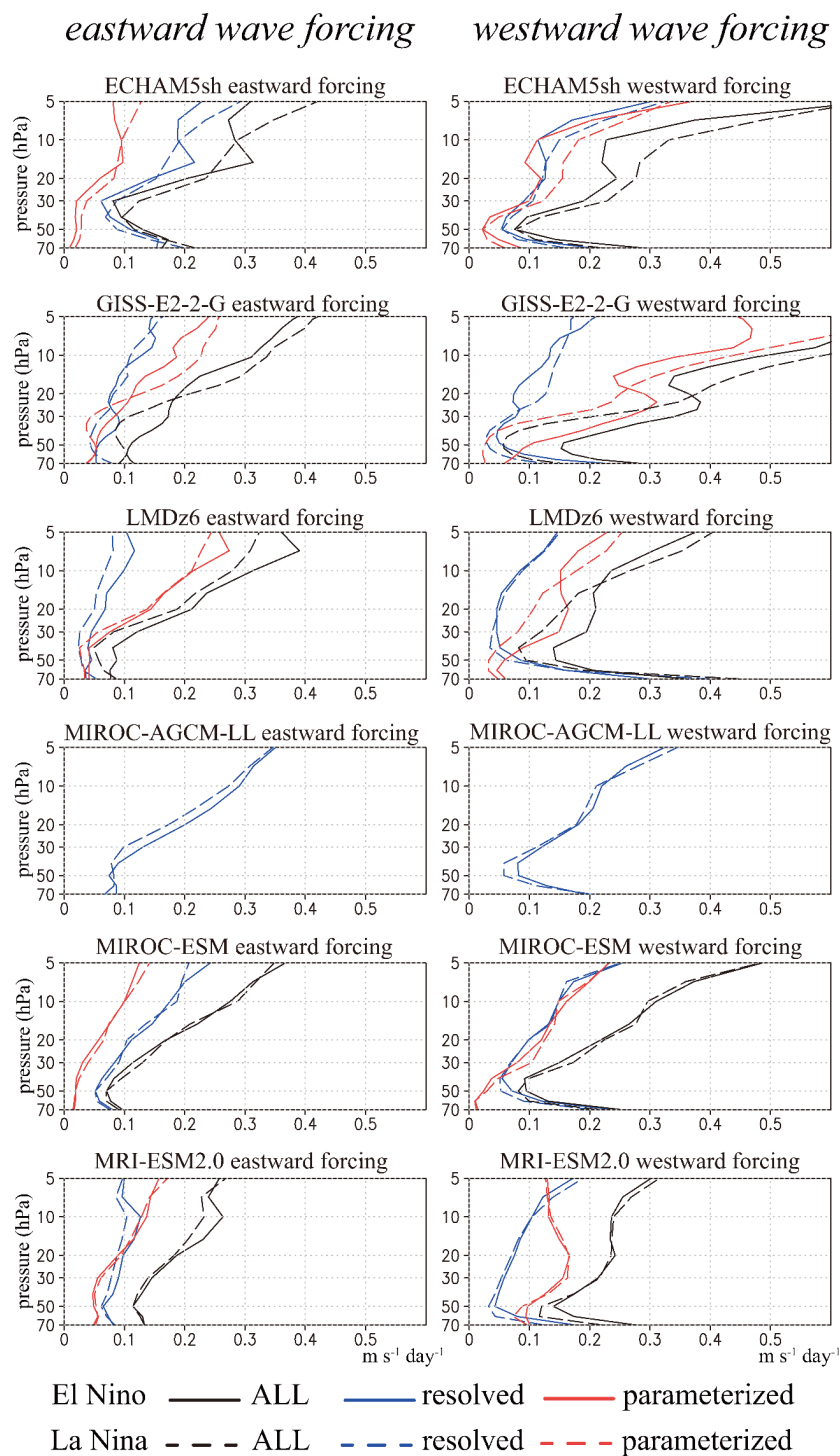
Fig. 14: Vertical profiles of the 10°S–10°N averaged eddy forcing of the zonal mean flow from (blue) resolved motions, (red) parameterized gravity waves and (black) their sum. Solid and dashed lines correspond to El Niño and La Niña runs.

5. Summary and concluding remarks

680   This study investigates how ENSO modulates the QBO using nine climate models that participated in QBOi . The experimental design builds upon Experiment 2 of QBOi phase-1 (see details in Butchart et al. 2018), but employs annually repeating SST patterns characteristic of El Niño and La Niña conditions. These SST anomalies, derived from observed data (1950-2016), were amplified to enhance their impact on QBO simulations. Notably, while other prescribed fields like sea ice 685 and ozone remained consistent between El Niño and La Niña runs, the imposed SST anomalies represent the sole difference in boundary conditions.

      The models differ in their representation of gravity wave processes, with five models (EC-EARTH, ECHAM, EMAC, MIROC-ESM, MRI) using fixed sources of parameterized gravity waves, three (GISS, LMDz, CESM1) incorporating variable gravity wave sources, and one (MIROC-AGCM) simulating the QBO solely through resolved wave dynamics. The study 690 analyzes a comprehensive suite of atmospheric variables from the model simulations, comparing them to reanalysis ERA-I data and CMAP precipitation data to evaluate the models' ability to capture observed ENSO modulations.

      A key finding is that all models consistently simulate longer QBO periods during La Niña compared to El Niño, in basic agreement with observations. In contrast, the modulation of QBO amplitude varies significantly among models, with GISS, LMDz and CESM1 (which used variable parameterized gravity wave sources) exhibiting the most pronounced 695 differences, while EC-EARTH, EMAC, MIROC-ESM and MRI show more modest changes. This finding contrasts the results from global warming experiments performed with the same QBOi models, in which projected QBO amplitude reductions were found to be much more consistent across models, but projected QBO period changes are inconsistent, showing shorter, longer, or even disappearing QBOs depending on the model (Richter et al. 2020a, b).

      Climatological mean-field differences associated with ENSO are qualitatively similar among models and broadly 700 consistent with observations. The models consistently capture the observed pattern of increased precipitation over the equator during El Niño, conducive to generating waves that can effectively interact with the QBO. Furthermore, differences in zonal-mean temperature and zonal wind patterns between El Niño and La Niña are evident, consistent with observed ENSO-related changes. Overall, these results indicate that the QBOi models successfully capture fundamental features of ENSO's influence on the QBO and mean climate, despite variations in the magnitude and details of these responses across different models.

705   Focusing on equatorial tropical upwelling, the models consistently show stronger upwelling during El Niño compared to La Niña, particularly up to approximately 10 hPa, with the most significant differences observed around 100-50 hPa. While these differences generally become smaller in the middle to upper stratosphere, LMDz and MRI stand out, exhibiting relatively larger differences due to the modulation extending to the deep branch of the BDC.

      The Walker circulation, characterized by easterly winds in the eastern hemisphere and westerly winds in the western 710 hemisphere, plays a significant role in filtering gravity waves propagating from the troposphere to the stratosphere. A weaker Walker circulation is evident during El Niño, potentially allowing for enhanced gravity wave propagation into the stratosphere due to reduced filtering. The representation of the Walker circulation during El Niño and La Niña shows some variation among

models, but the El Niño minus La Niña differences are very similar across models, with easterly anomalies over the central Pacific and westerly anomalies in other longitudes, consistent with observations.

715   The three models using Hines-type parameterized GWP (ECHAM, MIROC-ESM, and MRI-ESM) show similar patterns in longitudinal variations of eastward and westward fluxes during both El Niño and La Niña at 100 hPa. Eastward flux differences between El Niño and La Niña are notably positive around the central Pacific, with negative anomalies to the east and west. In contrast, westward flux differences are predominantly negative around the central Pacific. These variations align well with the differences in background zonal winds associated with the Walker circulation.

720   CESM1 exhibits a distinct, localized distribution of parameterized gravity wave fluxes compared to other models, likely due to its formulation of non-orographic GWP which features sources assumed dependent on the simulated adiabatic convective heating. This results in ENSO related variations influenced by both variable sources and Walker circulation filtering. The difference in eastward fluxes between El Niño and La Niña reveals positive values from the central to east Pacific, aligning with the location of maximum easterly anomalies of the Walker circulation. Conversely, negative values correspond to regions

725   of westerly anomalies in the mid-to-upper tropospheric Walker circulation at other longitudes. These differences show some resemblance to those observed in ECHAM, MIROC-ESM, and MRI. Unlike eastward waves, differences in westward fluxes in CESM1 exhibit large positive values in the eastern Pacific and negative anomalies in the western Pacific, associated with positive precipitation anomalies.

   Zonal wave forcing due to resolved and parameterized waves were composited based on QBO phase and these

730   composite fields display some differences among models. In particular, GISS and LMDz show larger eastward forcing due to resolved waves during El Niño compared to La Niña. Increased precipitation over the equator is a favorable condition for generating more Kelvin waves, which contribute to driving the westerly phase of the QBO. Both models, with variable parameterized gravity wave sources, have zonal wave forcing by parameterized waves that is much larger than that by resolved waves in both eastward and westward accelerations. In contrast, MIROC-ESM and MRI show smaller differences between

735   resolved and parameterized wave forcing. In MIROC-AGCM, a slight delay in the downward phase progression of the easterly phases during La Niña compared to El Niño is observed around 30-50 hPa, associated with smaller westward resolved wave forcing.

   The vertical profiles of mean eastward and westward forcing due to resolved and parameterized waves during El Niño and La Niña also exhibit inter-model differences. GISS and LMDz display the dominance of parameterized wave forcing over

740   resolved wave forcing, particularly above 30 hPa. Total wave forcing is generally stronger during El Niño in both GISS and LMDz. In MIROC-ESM, resolved eastward wave forcing surpasses parameterized forcing, while resolved and parameterized westward wave forcing is comparable. Differences in total wave forcing are small between El Niño and La Niña, except for slightly stronger westward forcing during El Niño between 40-70 hPa. In MRI, total eastward wave forcing during El Niño is significantly larger above 20 hPa, primarily driven by differences in resolved wave forcing. Parameterized westward wave

745   forcing dominates over resolved forcing, and differences in total wave forcing are observed below 40 hPa, with larger forcing

during El Niño. In MIROC-AGCM, both eastward and westward resolved wave forcing is stronger during El Niño than La Niña, with notable differences above 40 hPa for eastward forcing and 40-60 hPa for westward forcing.

The QBO period is consistently longer during La Niña than El Niño across all models. GISS and LMDz, which utilize parameterized GWPs with variable sources, exhibit significantly stronger wave forcing during El Niño and a correspondingly

750   larger ENSO modulation of the simulated QBO period. Of the nine models, EMAC, MIROC-ESM and MRI, which use Hines-type parameterized GWP schemes with fixed wave sources, show the weakest modulation of the QBO period by ENSO. While MIROC-AGCM, which relies solely on resolved waves, also produces a longer QBO period during La Niña, its results are likely affected by the model's T106 horizontal resolution. Two other models, EC-EARTH (fixed GWP sources) and CESM1 (variable GWP sources), exhibit larger QBO period modulations, but further analysis is limited by data availability. In contrast

755   to the consistent QBO period response, the sign of the ENSO effect on QBO amplitude varies among models. However, those employing variable parameterized gravity wave sources generally exhibit greater sensitivity of the QBO amplitude to ENSO than those using fixed sources (compare GISS, LMDz, and CESM1 to EC-EARTH, EMAC, MIROC-ESM, and MRI in Fig. 4).

While this analysis provides initial insights into the QBO response to ENSO through multi QBO-resolving model

760   comparison, further investigation is needed to fully understand the quantitative differences in QBO periods between El Niño and La Niña. This requires more detailed wave analyses, incorporating datasets with high temporal sampling. Notably such high frequency data could be applied to examine zonal wavenumber versus frequency spectra of EP-flux and precipitation, and to analyze parameterized wave forcing properties, including their three-dimensional variations.

Future research efforts should prioritize several key areas to enhance our understanding of the complex interplay

765   between ENSO and the QBO, ultimately contributing to more accurate climate change predictions. Firstly, different schemes of parameterized gravity waves lead to substantial differences among models. Comprehensive comparisons across various models are needed to refine these parameterizations and reduce these discrepancies. Secondly, further research is necessary to unravel the sources of gravity waves. While gravity waves are generated through various processes, the mechanisms behind their formation are not fully understood. This is particularly true for gravity waves generated by convective activity, which

770   requires further investigation. Finally, conducting much higher resolution simulations is essential. High-resolution simulations allow for more detailed analysis of gravity wave propagation and their impact on the QBO. In addition, comparing non-orographic parameterized gravity waves to observations, such as constant level balloons as done by Lott et al. (2024), would be valuable. By addressing these research priorities, we can gain a more comprehensive understanding of the complex interactions between ENSO and the QBO, which could contribute to more accurate climate change predictions.

775

Data availability

The JMA data and data description are provided in the web-pages:

El Niño monitoring and outlook: http://ds.data.jma.go.jp/tcc/tcc/products/elnino/index.html

Download El Niño Monitoring Indices: http://ds.data.jma.go.jp/tcc/tcc/products/elnino/index

780 Storage for the QBOi multi-model data set is provided by the Centre for Environmental Data Analysis (CEDA) whose data and processing service is called JASMIN. Interested users must obtain a JASMIN login account and take the necessary steps to access the QBOi group workspace within JASMIN, which contains the perpetual ENSO simulations.

Code availability

785 GFD-DENNOU Club codes are available at https://dennou-h.gfd-dennou.org/index.html.en

Grid Analysis and Display System (GrADS) is available at http://cola.gmu.edu/grads/

Author contributions

Competing interests

The authors declare that they have no conflict of interest.

795

Acknowledgement

810

References

Adachi, Y., Yukimoto, S., Deushi, M., Obata, A., Nakano, H., Tanaka, T. Y., Hosaka, M., Sakami, T., Yoshimura, H., Hirabara, M., Shindo, E., Tsujino, H., Mizuta, R., Yabu, S., Koshiro, T., Ose, T., and Kitoh, A.: Basic performance of a new earth system model of the Meteorological Research Institute (MRI-ESM1). Papers in Meteorology and Geophysics, 64, 1–19, doi:10.2467/mripapers.64.1, 2013.

Alexander M. J., Geller M., McLandress C., Polavarapu S., Preusse P., Sassi F., Sato K., Eckermann S. D., Ern M., Hertzog A., Kawatani Y., Pulido M., Semeniuk K., Shapiro I., Shephard G. G., Shiotani M., Sofieva V. F., and Wang L., Recent developments in gravity-wave effects in climate models and the global distribution of gravity-wave momentum flux from observations and models. Q. J. Roy. Meteor. Soc., 136, 1103–1124. https://doi.org/10.1002/qj.637, 2010.

Anstey, J. A. and Shepherd, T.: High-latitude influence of the quasi-biennial oscillation, Q. J. Roy. Meteor. Soc., 140, 1-21, https://doi.org/10.1002/qj.2132, 2014.

Anstey, J. A., Butchart, N., Hamilton, K. and Osprey, M.: The SPARC Quasi-Biennial Oscillation initiative. Q. J. Roy. Meteor. Soc., 148, 1455-1458, https://doi.org/10.1002/qj.3820, 2022.

Anstey, J. A., Osprey, S. M., Alexander, J., Baldwin, M. P., Butchart, N., Gray, L., Kawatani, Y., Newman, P. A., & Richter, J. H.: The Quasi-Biennial Oscillation: Impacts, Processes, and Projections. Nat. Rev. Earth Environ., https://doi.org/10.1038/s43017-022-00323-7, 2022.

Anstey, J. A., Simpson, I. R., Richter, J. H., Naoe, H., Taguchi, M., Serva, F., Gray, L. J., Butchart, N., Hamilton, K., Osprey, S., Bellprat, O., Braesicke, P., Bushell, A. C., Cagnazzo, C., Chen, C.-C., Chun, H.-Y., Garcia, R. R., Holt, L., Kawatani, Y., Kerzenmacher, T., Kim, Y.-H., Lott, F., McLandress, C., Scinocca, J., Stockdale, T. N., Versick, S., Watanabe, S., & Yoshida, K.: Teleconnections of the quasi-biennial oscillation in a multi-model ensemble of QBO-resolving models. Q. J. Roy. Meteor. Soc., https://doi.org/10.1002/qj.4048, 2021.

Baldwin M. P., Gray L. J., Dunkerton T. J., Hamilton K., Haynes P. H., Randel W. J., Holton J. R., Alexander M. J., Hirota I., Horinouchi T., Jones D. B. A., Kinnersley J. S., Marquardt C., Sato K., and Takahashi M., 2001. The Quasi-Biennial Oscillation. Rev. Geophys., 39, 179–229.

Baldwin M. P., and Dunkerton T. J., 2001. Stratospheric Harbingers of Anomalous Weather Regimes. Science, 294, 581–584.

Bushell, A. C., Anstey, J. A., Butchart, N., Kawatani, Y., Osprey, S. M., Richter, J. H., Serva, F., Braesicke, P., Cagnazzo, C., Chen, C.-C., Chun, H.-Y., Garcia, R. R., Gray, L. J., Hamilton, K., Kerzenmacher, T., Kim, Y.-H., Lott, F., McLandress, C., Naoe, H., Scinocca, J., Stockdale, T. N., Watanabe, S., Yoshida, K., & Yukimoto, S.: Evaluation of the Quasi-Biennial Oscillation in global climate models for the SPARC QBO-initiative. Q. J. Roy. Meteor. Soc., https://doi.org/10.1002/qj.3765, 2020.

Butchart, N., Anstey, J. A., Kawatani, Y., Osprey, S. M., Richter, J. H., & Wu, T.: QBO changes in CMIP6 climate projections. Geophys. Res. Lett., https://doi.org/10.1029/2019GL086903, 2020.

Butchart, N., Anstey, J., Hamilton, K., Osprey, S., McLandress, C., Bushell, A., Kawatani, Y., Kim, Y.-H., Lott, F., Scinocca, J., Stockdale, T., Bellprat, O., Braesicke, P., Cagnazzo, C., Chen, C.-C., Chun, H.-Y., Dobrynin, M., Garcia, R., Garcia-Serrano, J., Gray, L., Holt, L., Kerzenmacher, T., Naoe, H., Pohlmann, H., Richter, J., Scaife, A., Schenzinger, V., Serva, F., Versick, S., Watanabe, S., Yoshida, K., & Yukimoto, S.: Overview of experiment design and comparison of models participating in the SPARC Quasi-Biennial Oscillation initiative (QBOi). Geosci. Model. Dev., 11, 1009–1032, https://doi.org/10.5194/gmd-11-1009-2018, 2018.

Calvo, N., Garcia, R. R., Randel, W. J., & Marsh, D. R.: Dynamical Mechanism for the Increase in Tropical Upwelling in the Lowermost Tropical Stratosphere During Warm ENSO Events. J. Atmos. Sci., 67, 2331–2340, https://doi.org/10.1175/2010JAS3433.1, 2010.

DallaSanta, K., C. Orbe, D. Rind, L. Nazarenko, and J. Jonas. "Dynamical and trace gas responses of the quasi-biennial oscillation to increased CO2." J. Geophys. Res. Atmos. 126, no. 6 (2021): e2020JD034151.

Dee, D. P., Uppala, S. M., Simmons, A. J., Berrisford, P., Poli, P., Kobayashi, S., Andrae, U., Balmaseda, M. A., Balsamo, G., Bauer, P., Bechtold, P., Beljaars, A. C. M., van de Berg, L., Bidlot, J., Bormann, N., Delsol, C., Dragani, R., Fuentes, M., Geer, A. J., Haimberger, L., Healy, S. B., Hersbach, H., Hólm, E. V., Isaksen, L., Kållberg, P., Köhler, M., Matricardi, M., McNally, A. P., Monge-Sanz, B. M., Morcrette, J.-J., Park, B.-K., Peubey, C., de Rosnay, P., Tavolato, C., Thépaut, J.-N. and Vitart, F. (2011), The ERA-Interim reanalysis: configuration and performance of the data assimilation system. Q.J.R. Meteorol. Soc., 137: 553–597. doi: 10.1002/qj.828

Domeisen, D. I. V., Garfinkel, C. I. and Butler, A. H., : The teleconnection of El Niño Southern Oscillation to the stratosphere. Rev. Geophys., 57, 5-47, 2019.

Dunkerton, T. J., Modification of stratospheric circulation by trace constituent changes? J. Geophys. Res., 88, 10831–10836. 1983.

Dunkerton, T. J., & Delisi, D. P.: Climatology of the Equatorial Lower Stratosphere. J. Atmos. Sci., 42, 376–396, https://doi.org/10.1175/1520-0469(1985)042<0376:COTELS>2.0.CO;2, 1985.

Dunkerton T. J.: The role of gravity waves in the quasi-biennial oscillation. J. Geophys. Res.-Atmos., 102, 26053–26076, 1997

Evan, S., Alexander, M. J., & Duhia, J.: Model Study of Intermediate-Scale Tropical Inertia-Gravity Waves and Comparison to TWP-ICE Campaign Observations. J. Atmos. Sci., 69, 591–610, https://doi.org/10.1175/JAS-D-11-051.1, 2012.

Geller, M.A., Shen, W., Zhang, M., and Tan, W.-W., Calculations of the stratospheric quasi-biennial oscillation for time-varying wave forcing, J. Atmos. Sci., 54, 883–894, https://doi.org/10.1175/1520-0469(1997)054<0883:COTSQB>2.0.CO;2 , 1997.

Giorgetta M. A., Manzini E., Roeckner E., Esch M., and Bengtsson L.: Climatology and forcing of the quasi-biennial oscillation in the MAECHAM5 model. J. Climate, 19, 2882-3901, https://doi.org/10.1175/JCLI3830.1, 2002

Hamilton, K., On the quasi-decadal modulation of the stratospheric QBO period, J. Clim., 15, 2562–2565. https://doi.org/10.1175/1520-0442(2002)015<2562:OTQDMO>2.0.CO;2, 2002.

Hamilton, K., Wilson, R. J., & Hemler, R.: Middle Atmosphere Simulated With High Vertical and Horizontal Resolution Versions of a GCM: Improvement in the Cold Pole Bias and Generation of a QBO-like Oscillation in the Tropics. J. Atmos. Sci., 56, 3829–3846, https://doi.org/10.1175/1520-0469(1999)056<3829:MASWVH>2.0.CO;2, 1999.

Holt, L., Lott, F., Garcia, R., Kiladis, G. N., Anstey, J. A., Braesicke, P., Bushell, A. C., Butchart, N., Cagnazzo, C., Chen, C.-C., Chun, H.-Y., Kawatani, Y., Kerzenmacher, T., Kim, Y.-H., McLandress, C., Naoe, H., Osprey, S., Richter, J. H., Scaife, A. A., Scinocca, J., Serva, F., Versick, S., Watanabe, S., & Yukimoto, S.: An Evaluation of Tropical Waves and Wave Forcing of the QBO in the QBOi Models. Q. J. Roy. Meteor. Soc., https://doi.org/10.1002/qj.3827, 2020.

Kane, R.P., Comparison of stratospheric zonal winds and El Niño–Southern Oscillation in recent decades, Int. J. Climatol., 24, 525–532. 2004.

Kawatani, Y., Tsuji, K., & Takahashi, M.: Zonally Non-Uniform Distribution of Equatorial Gravity Waves in an Atmospheric General Circulation Model. Geophys. Res. Lett., 32, L23815, https://doi.org/10.1029/2005GL024068, 2005.

Kawatani, Y., Takahashi, M., Sato, K., Alexander, S. P., & Tsuda, T.: Global Distribution of Atmospheric Waves in the Equatorial Upper Troposphere and Lower Stratosphere: AGCM Simulation of Sources and Propagation. J. Geophys. Res., 114, D01102, https://doi.org/10.1029/2008JD010374, 2009.

Kawatani, Y., Sato, K., Dunkerton, T. J., Watanabe, S., Miyahara, S., & Takahashi, M.: The Roles of Equatorial Trapped Waves and Internal Inertia-Gravity Waves in Driving the Quasi-biennial Oscillation. Part I: Zonal Mean Wave Forcing. J. Atmos. Sci., 67, 963–980, https://doi.org/10.1175/2009JAS3222.1, 2010a.

Kawatani, Y., Sato, K., Dunkerton, T. J., Watanabe, S., Miyahara, S., & Takahashi, M.: The Roles of Equatorial Trapped Waves and Internal Inertia-Gravity Waves in Driving the Quasi-biennial Oscillation. Part II: Three-Dimensional Distribution of Wave Forcing. J. Atmos. Sci., 67, 981–997, https://doi.org/10.1175/2009JAS3223.1, 2010b.

Kawatani, Y., Hamilton, K., & Watanabe, S.: The Quasi-Biennial Oscillation in a Doubled CO_2 Climate. J. Atmos. Sci., 68, 265–283, https://doi.org/10.1175/2010JAS3623.1, 2011.

Kawatani, Y., & Hamilton, K.: Weakened stratospheric Quasi-biennial Oscillation driven by increased tropical mean upwelling. Nature, 497, 478–481, https://doi.org/10.1038/nature12140, 2013.

Kawatani, Y., Hamilton, K., Sato, K., Dunkerton, T. J., Watanabe, S., & Kikuchi, K.: ENSO Modulation of the QBO: Results From MIROC Models With and Without Non-orographic Gravity Wave Parameterization. J. Atmos. Sci., 76, 3893–3917, https://doi.org/10.1175/JAS-D-19-0163.1, 2019.

Kidston, J., Scaife, A. A., Hardiman, S. C., Mitchell, D. M., Butchart, N., Baldwin, M. P., & Gray, L. J.: Stratospheric Influence on Tropospheric Jet Streams, Storm Tracks and Surface Weather. Nat. Geosci., 8, 433–440, https://doi.org/10.1038/ngeo2424, 2015.

Lindzen, R. S., & Holton, J. R.: A Theory of the Quasibiennial Oscillation. J. Atmos. Sci., 25, 1095–1107, https://doi.org/10.1175/1520-0469(1968)025<1095:ATOTQO>2.0.CO;2, 1968.

Lott, F., Rani, R., McLandress, C., Podglajen, A., Bushesll, A., Bramberger, M., Lee, H.-K., Alexander, J., Anstey, J., Chun, H.-Y., Herzog, A., Butchart, N., Kim, Y.-H., Kawatani, Y., Legras, B., Manzini, E., Naoe, H., Osprey, S., Plougonven,

910 R., Pohlmann, H., Richter, J. H., Scinocca, J., Garcia-Serrano, J., Serva, F., Stockdale, F., Versick, S., Watanabe, S., Yoshida, K.: Comparison between non orographic gravity wave parameterizations used in QBOi models and Strateole 2 constant level balloons, Q. J. Roy. Meteor. Soc., accepted, 2024.

Lu, J., Chen, G. and D. M. W. Frierson: Response of the Zonal Mean Atmospheric Circulation to El Niño versus Global Warming, J. Climate, 21, 5835-5851, https://doi.org/10.1175/2008JCLI2200.1, 2008.

915 Naoe, H., and Yoshida, K.: Influence of quasi-biennial oscillation on the boreal winter extratropical stratosphere in QBOi experiments, Q. J. Roy. Meteor. Soc., 145, 2755-2771, https://doi.org/10.1002/qj.3591, 2019.

Naujokat, B., An update of the observed Quasibiennial Oscillation of the stratospheric zonal winds over the tropics. J. Atmos. Sci., 43, 1873-1877, https://doi.org/10.1175/1520-0469(1986)043<1873:AUOTOQ>2.0.CO;2 , 1986.

Quiroz, R.S., Period modulation of the stratospheric Quasibiennial Oscillation. Mon. Wea. Rev., 109, 665-674, 920 https://doi.org/10.1175/1520-0493(1981)109<0665:PMOTSQ>2.0.CO;2, 1981.

Randel, W. J., Garcia, R. R., Calvo, N., & Marsh, D.: ENSO Influence on Zonal Mean Temperature and Ozone in the Tropical Lower Stratosphere. Geophys. Res. Lett., 36, L15822, https://doi.org/10.1029/2009GL039343, 2009.

Richter, J. H., Butchart, N., Kawatani, Y., Bushell, A. C., Holt, L., Serva, F., Anstey, J. A., Simpson, I. R., Osprey, S. M., Hamilton, K., Braesicke, P., Cagnazzo, C., Chen, C.-C., Garcia, R. R., Gray, L. J., Kerzenmacher, T., Lott, F., McLandress, 925 C., Naoe, H., Scinocca, J., Stockdale, T. N., Versick, S., Watanabe, S., Yoshida, K., & Yukimoto, S.: Response of the Quasi-Biennial Oscillation to a Warming Climate in Global Climate Models. Q. J. Roy. Meteor. Soc., https://doi.org/10.1002/qj.3749, 2020.

Rind, D., Jonas, J., Kelley, M., Lacis, A., Russell, G., Schmidt, G. A., & Ruedy, R.: GISS Model E2.2: Description, Evaluation and Attribution of 20th Century Climate Change. J. Adv. Model. Earth Sy., 12, e2019MS001915, 930 https://doi.org/10.1029/2019MS001915, 2020.Salby, M., and Callaghan, P., Connection between the solar cycle and the QBO: The missing link, J. Clim., 13, 2652–2662, https://doi.org/10.1175/1520-0442(1999)012<2652:CBTSCA>2.0.CO;2, 2000.

Schirber, S., Influence of ENSO on the QBO: Results from an ensemble of idealized simulations. J. Geophys. Res., 120, 1109–1122, https://doi.org/10.1002/2014JD022460, 2015.

935 Serva, F., Cagnazzo, C., Christiansen, B., and S. Yang: The influence of ENSO events on the stratospheric QBO in a multi-model ensemble. Clim Dyn 54, 2561–2575, https://doi.org/10.1007/s00382-020-05131-7, 2020.

Simpson, I. R., Sigmond, M., and Shepherd, T. G., Dynamics of the lower stratospheric circulation response to ENSO. J. Atmos. Sci., 68, 2537–2556, https://doi.org/10.1175/JAS-D-11-05.1, 2011.

Stockdale, T. N., Kim, Y.-H., Anstey, J. A., Palmeiro, F. M., Butchart, N., Scaife, A. A., Andrews, M., Bushell, A. C., Dobrynin, 940 M., Garcia‐Serrano, J., Hamilton, K., Kawatani, Y., Lott, F., McLandress, C., Naoe, H., Osprey, S. M., Pohlmann, H., Scinocca, J., Watanabe, S., Yoshida, K., and Yukimoto, S : Prediction of the quasi‐biennial oscillation with a multi‐model ensemble of QBO‐resolving models. Q. J. Roy. Meteor. Soc., https://doi.org/10.1002/qj.3919, 2020.

Stevens, B., Giorgetta, M., Esch, M., Mauritsen, T., Crueger, T., Rast, S., Salzmann, M., Schmidt, H., Bader, J., Block, K., Brokopf, R., Fast, I., Kinne, S., Kornblueh, L., Lohmann, U., Pincus, R., Reichler, T., Roeckner, E., and others: Atmospheric component of the MPI-M Earth System Model: ECHAM6. J. Adv. Model. Earth Sy., 5, 1–28, https://doi.org/10.1002/jame.20015, 2013

Taguchi, M.: Observed connection of the stratospheric quasi-biennial oscillation with El Niño–Southern Oscillation in radiosonde data, J. Geophys. Res., 115, D18120, https://doi.org/10.1029/2010JD014325, 2010.

Trenberth, K. E., Branstator, G. W., Karoly, D., Kumar, A., Lau N.-C., Ropelewski, C.: Progress during TOGA in understanding and modeling global teleconnections associated with tropical sea surface temperatures, J. Geophys. Res. Atmos., 103, 14167-14510, https://doi.org/10.1029/97JC01444, 1998.

Vecchi, G. A. and B. J. Soden: Global Warming and the Weakening of the Tropical Circulation, J. Climate, 20, 4316-4340, https://doi.org/10.1175/JCLI4258.1, 2007.

Watanabe, S., Kawatani, Y., Tomikawa, Y., Miyazaki, K., Takahashi, M., and Sato, K.: General aspects of a T213L256 middle atmosphere general circulation model. J. Geophys. Res., 113, D12110, doi:10.1029/2008JD010026, 2008.

Watanabe, S. and Kawatani, Y.: Sensitivity of the QBO to mean tropical upwelling under a changing climate simulated by an Earth system model, J. Meteor. Soc. Japan., 90A, 351-360., https://doi.org/10.2151/jmsj.2012-A20, 2012.

Xie, P., and Arkin, P. A.: Global Precipitation: A 17-year monthly analysis based on gauge observations, satellite estimates, and numerical model outputs. Bull. Amer. Meteor. Soc., 78, 2539–2558, https://doi.org/10.1175/1520-0477(1997)078<2539:GPAYMA>2.0.CO;2, 1997.

Yoo, C., and Son, S.-W.: Modulation of the boreal wintertime Madden-Julian oscillation by the stratospheric quasi-biennial oscillation. Geophys. Res. Lett., 43, 1392–1398, https://doi.org/10.1002/2016GL067762, 2016.

Yukimoto, S., Adachi, Y., Hosaka, M., Sakami, T., Yoshimura, H., Hirabara, M., Tanaka, T. Y., Shindo, E., Tsujino, H., Deushi, M., Mizuta, R., Yabu, S., Obata, A., Nakano, H., Koshiro, T., Ose, T., and Kitoh, A.: A new global climate model of the Meteorological Research Institute: MRI-CGCM3 — Model description and basic performance —. J. Meteor. Soc. Japan, 90A, 23–64, doi:10.2151/jmsj.2012-A02, 2012.

Yukimoto, S., Kawai, H., Koshiro, T., Oshima, N., Yoshida, K., Urakawa, S., Tsujino, H., Deushi, M., Tanaka, T., Hosaka, M., Yabu, S., Yoshimura, H., Shindo, E., Mizuta, R., Obata, A., Adachi, Y., and Ishii, M.: The Meteorological Research Institute Earth System Model Version 2.0, MRI-ESM2.0: Description and Basic Evaluation of the Physical Component. J. Meteor. Soc. Japan, 97, 931–965, doi:10.2151/jmsj.2019-051, 2019.

Yuan, W., Geller, M. A., and Love, P. T.: ENSO influence on QBO modulations of the tropical tropopause. Q. J. R. Meteorol. Soc., 140, 1670–1676, https://doi.org/10.1002/qj.2247, 2014.